Measurement and Modeling of Broadband Millimeter-Wave Signal Propagation Between Intelligent Vehicles

January 2021

A Research Report from the Pacific Southwest Region University Transportation Center

Andreas F. Molisch, Principal Investigator

Hussein Hammoud, Ph.D. Student

Yuning Zhang, Project Assistant

TECHNICAL REPORT DOCUMENTATION PAGE

1. Report No. PSR-18-08	**2. Government Accession No.** N/A	**3. Recipient's Catalog No.** N/A
4. Title and Subtitle Measurement and Modeling of Broadband Millimeter-Wave Signal Propagation Between Intelligent Vehicles		**5. Report Date** January 2021 **6. Performing Organization Code** N/A
7. Author(s) Andreas F. Molisch https://orcid.org/0000-0002-4779-4763 Hussein Hammoud Yuning Zhang		**8. Performing Organization Report No.** PSR-18-08
9. Performing Organization Name and Address METRANS Transportation Consortium University of Southern California 650 Childs Way, RGL 216 Los Angeles, CA 90089-0626		**10. Work Unit No.** N/A **11. Contract or Grant No.** USDOT Grant 69A3551747109
12. Sponsoring Agency Name and Address U.S. Department of Transportation Office of the Assistant Secretary for Research and Technology 1200 New Jersey Avenue, SE, Washington, DC 20590		**13. Type of Report and Period Covered** Final White Paper (Sept. 2017 – March 2019) **14. Sponsoring Agency Code** USDOT OST-R

15. Supplementary Notes
Project webpage: https://www.metrans.org/research/measurement-and-modeling-of-broadband-millimeter-wave-signal-propagation-between-intelligent-vehicles

16. Abstract

Communications between vehicles is one of the most important prerequisites for inter-vehicle coordination, a key feature needed to enable autonomous and semi-autonomous driving, from an efficiency, convenience and safety perspective. Such communication will have to be done with very low latency, which lead the industry into looking at mm-wave bands, where much larger chunks of bandwidth are available. To understand the different implications of mm-wave propagation in Vehicle-to-Vehicle scenarios (V2V), channel sounders have to be built, and double-directional channel models have to be extracted, in a wide variety of scenarios and environments. In the line of this project, we perform measurement campaigns for a variety of situations, based on a novel channel sounder capable of measuring a full double-directional channel. We also provide extracted parameters such as the directional RMS delay spread and angular spreads on both Tx and Rx, that are a requirement for intelligent vehicles system development.

17. Key Words Safety, Connected Vehicles, Autonomous Vehicles, Wireless Technology, Inter-vehicle Coordination	**18. Distribution Statement** No restrictions.		
19. Security Classif. (of this report) Unclassified	**20. Security Classif. (of this page)** Unclassified	**21. No. of Pages** 61	**22. Price** N/A

Contents

List of Figures

About the Pacific Southwest Region University Transportation Center

The Pacific Southwest Region University Transportation Center (UTC) is the Region 9 University Transportation Center funded under the US Department of Transportation's University Transportation Centers Program. Established in 2016, the Pacific Southwest Region UTC (PSR) is led by the University of Southern California and includes seven partners: Long Beach State University; University of California, Davis; University of California, Irvine; University of California, Los Angeles; University of Hawaii; Northern Arizona University; Pima Community College.

The Pacific Southwest Region UTC conducts an integrated, multidisciplinary program of research, education and technology transfer aimed at improving the mobility of people and goods throughout the region. Our program is organized around four themes: 1) technology to address transportation problems and improve mobility; 2) improving mobility for vulnerable populations; 3) Improving resilience and protecting the environment; and 4) managing mobility in high growth areas.

U.S. Department of Transportation (USDOT) Disclaimer

The contents of this report reflect the views of the authors, who are responsible for the facts and the accuracy of the information presented herein. This document is disseminated in the interest of information exchange. The report is funded, partially or entirely, by a grant from the U.S. Department of Transportation's University Transportation Centers Program. However, the U.S. Government assumes no liability for the contents or use thereof.

California Department of Transportation (CALTRANS) Disclaimer

The contents of this report reflect the views of the authors, who are responsible for the facts and the accuracy of the information presented herein. This document is disseminated under the sponsorship of the United States Department of Transportation's University Transportation Centers program, in the interest of information exchange. The U.S. Government and the State of California assumes no liability for the contents or use thereof. Nor does the content necessarily reflect the official views or policies of the U.S. Government and the State of California. This report does not constitute a standard, specification, or regulation. This report does not constitute an endorsement by the California Department of Transportation (Caltrans) of any product described herein.

Disclosure

Principal Investigator Andreas F. Molisch, as well as PhD student Hussein Hammoud, MS student (later resource employee Yuning Zhang, conducted this research titled, "Measurement and Modeling of Broadband Millimeter-Wave Signal Propagation Between Intelligent Vehicles" at the Ming Hsieh Department of Electrical and Computer Engineering, Viterbi School of Engineering, University of Southern California. The research took place from August 2018 to Jan 2021 and was funded by a grant from the METRANS in the amount of $ 100,000. The research was conducted as part of the Pacific Southwest Region University Transportation Center research program.

Acknowledgement

We would like to thank the METRANS project, and in particular Genevieve Giuliano, Cort Brinkerhoff and Katrina Soriano for their kind help in handling of the Covid situation. We are grateful to Prof. Katsu Haneda from Aalto University for loaning us up/downconverters for the experiments. The many discussions, helpful suggestions, and excellent collaboration with Prof. Christoph Mecklenbrauker, Dr. Thomas Zemen, Prof. Jiri Blumenthal, Markus Hofer, Herbert Groll, and our other collaborators at TU Wien, AIT, and TU Brno are gratefully acknowledged. We would also like to thank our colleagues Jorge Gomez and Guillermo Castro, PhD students in our group at USC, and former PhD Student Dr. Seun Sangodoyin (now Georgiatech) for their help in the system design and the measurements campaign.

Abstract

Communications between vehicles is one of the most important prerequisites for inter-vehicle coordination, a key feature needed to enable autonomous and semi-autonomous driving, from an efficiency, convenience and safety perspective. Such communication will have to be done with very low latency, which lead the industry into looking at mm-wave bands, where much larger chunks of bandwidth are available. To understand the different implications of mm-wave propagation in Vehicle-to-Vehicle scenarios (V2V), channel sounders have to be built, and double-directional channel models have to be extracted, in a wide variety of scenarios and environments. In the line of this project, we perform measurement campaigns for a variety of situations, based on a novel channel sounder capable of measuring a full double-directional channel. We also provide extracted parameters such as the directional RMS delay spread and angular spreads on both Tx and Rx, that are a requirement for intelligent vehicles system development.

Measurement and Modeling of Broadband Millimeter-Wave Signal Propagation Between Intelligent Vehicles

Executive Summary

Mm-wave communications offers large bandwidth and with it associated high data rates. It is thus well suited for vehicle-to-vehicle (V2V) communications, which in the future will exchange observations (video) and other driving data between vehicles. However, mm-wave propagation also suffers from various impairments, such as blockage, delay dispersion, etc. In order to assess the potential of mm-wave based V2V communications systems, a thorough understanding of mm-wave channels in V2V settings is required. In particular, since mm-wave systems require beamforming to overcome large isotropic pathloss, directionally resolved channel measurements and models are required.

To be able to perform V2V channel modelling and the extraction of relevant parameters for system development, the first step is to build a channel sounder, capable of delivering such parameters. For our project, we designed and built a channel sounder that can operate at 60 GHz, with a bandwidth of 200 MHz (that can be increased up to 1 GHz), and that is able to measure a continuous real-time capture of the propagation channel. The transmitter is continuously radiating a custom-designed multi-tone sequence, while the receiver is capturing at an interrupted intervals of 200 μ s each. The double-directional sounding of the channel was made possible by a mechanically rotating beams architecture. The fundamental principle of this architecture is based on a SISO (single-input - single-output) transmission into a narrow cone (directional range), whose center angle is changed with a very fast mechanical rotation. These mechanical rotations are captured using a photo-electric sensor, allowing a one-to-one mapping between the captured channel response and the corresponding angular direction.

Using the designed sounder, we have performed measurements in a variety of environments, including both LOS and NLOS situations, intended as a proof-of-principle, to check for any problems with the design and form a basis for later corrections before a more extended measurement campaign. Problems that were discovered during the data processing include an occasionally-faulty photoelectric sensor on the receiver side in addition to software-induced delays in between receiver captures. While we were able to solve all these problems and adjustments were made on the system in a laboratory enviornment to make sure we do not suffer from such issues again, we were not able to proceed with the intended plan of redoing the measurement campaigns due to the COVID-19 pandemic and the resulting restrictions on laboratory work and particular measurement campaigns that require close interactions of multiple people. However, through careful post-processing of the measurement data, we were able to extract meaningful data and showed physically reasonable explanation for these results. Such results include information about the directional

power delay profile and corresponding RMS delay spread, which are the parameters necessary for the design of V2V operating parameters such as equalizer length or cyclic prefix. We found that in most situations, this directional delay spread is on the order of 1-3 ns. We also extracted joint Tx-Rx Angular Power Spectra and the corresponding angular spreads, that were found to be quite significant. Such analysis also showed that even in a NLOS scenario, where a truck is blocking the LOS between the Tx and the Rx, reflections via other objects in the vicinity can carry the most significant energy and allow to maintain communications. We stress that such insights cannot be easily obtained from the conventional "fixed-horn" measurements performed in previous mmWave V2V campaigns.

The next planned stage out of our work is to re-calibrate the new setup after all the adjustments on the system, and then to re-do not only the scenarios that are evaluated in this report, but to perform more extensive measurement campaigns with longer trajectories and stronger variations of the distances between the Tx and the Rx. While these measurements could not be performed before the due date of this final report, we will still execute them and publish the results in suitable journals and/or conferences, and will provide the details of the results to METRANS.

1 Introduction

Intelligent vehicles, enabling autonomous and semi-autonomous driving, are expected to become the dominant mode of transportation over the next 20 years. While a large part of the research concentrates on the use of on-board sensors and their intelligent processing, another important avenue is communications *between* vehicles that allows coordination of driving maneuvers.

Inter-vehicle coordination is important both for the improvement of traffic flow, and for accident reduction. From a traffic flow point of view, a simple example occurs during lane change: if a car that wants to merge into another lane can let the vehicles already-present in that lane know about its intentions, "squeezing" in between two cars can be done with much less inter-vehicle distance than if unpredictable acceleration/deceleration of the cars have to be planned for. More generally, convoys of cars and trucks, driving with small inter-vehicle distances, and thus enhancing fuel efficiency and traffic flow, are enabled through reliable inter-vehicle communications. From a safety point of view, inter-vehicle communications are key in providing information for obstacles and dangers that are out of "line-of-sight" of the on-board sensors (radar, lidar, camera) of a particular car, but can be seen by the sensors of another car. For example, a tree blocking a lane "around a bend" can be communicated by another vehicle that is around the corner. Similarly, "chain-reaction" rear-ending accidents can be avoided if the presence of a stalled vehicle can be communicated over larger distances.

A first step towards vehicle coordination has been made by the introduction of the WAVE (IEEE 802.11p) standard for inter-vehicle communication, which is started deployment in new vehicles starting this year. It operates in the 5.9 GHz band, where 10 MHz spectrum has been assigned to this service. However, the data rates enabled by this standard are quite low. Not only is the available bandwidth small, but the spectral resources have to be shared by all vehicles within the communication radius (around 300m) - which, on a busy city freeway, can be on the order to 1000 vehicles. Thus, only condensed information (velocity, braking state, etc.) can be communicated. Similarly, 3GPP has developed a vehicular communication mode based on their "Sidelink" peer-to-peer communications mode of LTE; it has been suggested for use in the same 5.9 GHz band, and suffers from similar constraints.

To improve the information from other cars and merge it with the information of the on-board sensors, it would be desirable to send the raw sensor data (such as the current lidar scans) to the surrounding cars [27]. Since this transmission has to be done with low latency, the most efficient data compression algorithms, which introduce significant latency, cannot be used. Thus, the data rate at which the transmissions have to occur, increase to 100-1000 Mbit/s per car. This is clearly impossible within the constraints of the current bandwidth assignments. Instead, these new applications will have to work at mm-wave frequencies, where several Gigahertz of bandwidth are available [10, 14, 27]. In particular, in the US, the FCC has assigned

in 2016 a total of 14 GHz of spectrum between 20 and 100 GHz for new communications applications. The potential of vehicle-to-vehicle (V2V) communications in the mm-wave band has also been recognized by the cellular industry, which is exploring such systems as part of the 5G standardization effort in 3GPP (the worldwide cellular standardization body). V2V (and more generally V2X) communications is recognized as one of the most important application areas ("verticals", in 3GPP parlance) that will drive the adoption of 5G [8, 37, 7].

The prerequisite for the development of new V2V systems is the understanding of the V2V propagation channel [21]. Only by knowing such key numbers as path loss, shadowing that might lead to outage, delay dispersion, and angular spread (which determines the potential improvement through multiple-antenna systems) can a reasonable system development be done. Yet, at the current time, much of that information is unknown. As outlined in Sec. 1.2, some measurement campaigns have been performed, but those were done with measurement setups that do now allow extraction of all relevant information. In particular, it is well known that mm-wave systems require adaptive arrays to compensate for the large free-space pathloss; yet, existing measurements do not allow to extract the channel properties determining the applicability of such arrays (also known as "directional channel properties"). This is due to limitations in existing channel measurement equipment (also known as "channel sounders"). Furthermore, measurements in many practically important scenarios are completely missing. While 3GPP is currently discussing a channel model as the basis for their further activities in this space, it is not based on many measurements and mainly extrapolates sub-6 GHz models to the mm-wave range, even though the propagation mechanisms at those frequencies are significantly different. Several papers in the academic literature have pointed out these and other shortcomings.

The goal of the reported project was to remedy these deficiencies, and to (i) perform measurement campaigns in a variety of environments based on a novel channel sounder that is capable of measuring all relevant information, and (ii) develop channel models that are in agreement with physical reality, and provide all the information required for system development.

1.1 State of the art

Channel sounding is the process of exciting the propagation channel with a known signal, measuring the received signal, and from this extracting the “channel response”. The most general channel sounding answers the question: “if we excite the channel by a short pulse of known amplitude, transmitted in a particular direction, then what are the amplitudes, delays, and angles of the signal components (multi-path components, MPCs) arriving at the receiver?” Depending on the capabilities of the channel sounder, the information might be restricted to obtaining only the delay of the MPCs, or possibly only the overall received power. Specifically, if the transmitter and/or receiver has omni-directional antennas, then no information about the

directions of the MPCs can be obtained. Narrow-band measurements, where the excitation signal covers only a small bandwidth, do not allow to extract information about the delays of the MPCs, though they do provide a better signal-to-noise ratio, and thus a larger possible measurement range between transmitter and receiver.

There is a rich literature for V2V channel measurements and modeling below 6 GHz. Since it is not directly applicable to the proposed project, we only briefly mention that V2V measurement campaigns have been carried out in various propagation environments, *urban*, *suburban*, *highway*, and *rural*; see e.g., [42, 32, 24, 20, 9, 2, 26] as well as [23], [22] and references therein.

The campaigns are mostly conducted by letting two vehicles drive in the same or in opposite directions on the same street. These campaigns usually establish average pathloss and delay dispersion models from the measured results; the validity of the Wide-Sense-Stationary Uncorrelated Scattering assumption has been investigated in [33, 3, 4]. Only few measurements provide the directional characteristics of the propagation channels, even though these are very important for multi-antenna structures. [34] proposes a V2V channel model based on measurements conducted in Helsinki, Finland. The DRIVEWAY campaign in Lund, Sweden, e.g., [1] and our measurements in Los Angeles, CA, e.g., [46] report analyses and models based on high-resolution directional evaluations.

V2V propagation channel measurements *for the mm-wave band* have been done since the early 2000s, especially in Japan. Many of those existing measurements were done with omni-directional antennas at the transmitter (Tx) and the receiver (Rx). This allows to gather MPCs from all directions, though at the same time the directional information is lost. The main information gathered from these measurement campaigns is the pathloss and shadowing.

A further key drawback of the omni-directional measurements is the high free-space pathloss inherent in mm-wave frequencies and thus a small maximum distance between Tx and Rx. This problem can be mitigated by using horn antennas at both link ends; the antenna gains of those antennas increase the SNR and thus allow measurements over larger distances. A number of measurement campaigns have been performed with horn antennas that have a fixed orientation (the antenna in the lead car pointing backwards, and the antenna in the following car pointing forwards, so that measurements can be done when the two cars are driving in convoy. However, a key drawback of the measurement setup is that MPCs that are arriving (or departing) at angles outside the beamwidth of the horn antenna are not measured at all. Thus, when the "direct" connection between lead and follow car is shadowed off, the channel sounder does not record any useful information. In reality, however, other MPCs could "bounce" off a house wall and get reflected to the Rx, where they could be received by a well-designed adaptive array. The fixed horn antenna setup thus provides

an incomplete picture of the propagation situation and might blind system developers to promising avenues.

Due to these issues, existing measurements only serve to extract fading/shadowing/pathloss statistics, e.g., [39, 40, 18, 48, 38, 43]. The impact of blocking vehicles between Tx and Rx was investigated in [47, 41]; diffraction over, as well as under, the car is shown to be important, though no measurements of the impact on angular spectrum (only overall pathloss) is investigated. A review of mm-wave channels for V2V can be found in [44]. However, the measurements mentioned there, just like the other measurements in this paragraph, do not describe the change of angular characteristics of the channel.

There are several more recent papers discussing mmWave channel models for V2V. Firstly, [17] provides an overview of the state of the art, as well as numerous references. References [36, 35] consider V2V communications on highways. They state that several previous models use simplified and predetermined distribution for the transceivers, which take into account the directionality of antenna pattern, but may discard the effects of reflection, diffraction and transmission through obstacles. Refs. [36, 35] overcome these limitations by using extensive ray-launching (RL) that not only consider the more complicated scenarios, but also specify the criteria for the directionality of the pattern to synthesize directional path loss. Other articles such as [28] claim that the massive deployment of V2V systems, which must support high data-rate, may lead to significant interference, which in turn affects the signal transmission performance. It comprehensively approximates the interference that caused by the side lane vehicle by using two-dimensional stochastic models for both highway and urban environment.

Ref. [13] discusses the channel model that 3GPP offered for both highway and urban scenario. It points out that the model does not adequately model the density of traffic and blockers, and lacks the effect of directional transmissions, confirming our above statement that the current 3GPP model is insufficient.

Refs. [25] and [19] describe the difference between the response when the antenna is installed at different locations on a vehicle at 28 GHz. However, the discussion is not directly applicable to our measurements, since these papers consider sedans, while our measurements were done with pick-up trucks. The impact of blockage by other cars is discussed in [6], and in particular comparisons between blocking in different frequency ranges is provided. Note that all of the measurements mentioned in this paragraph are done with static setups.

In terms of dynamic measurements, fading characteristics (with fixed-direction antennas) at 73 GHz were measured in [45]. A channel sounder based on phased arrays, and some sample measurements, were presented in a recent (Dec. 2020) conference contribution [11].

2 Construction of the Channel Measurement Test Equipment

For our measurements, we required a channel sounder that has the following properties:

- Operation at 60 GHz, the envisioned operating frequency.
- Wideband operation (bandwidth at least 100 MHz), so that sufficient delay resolution is provided.
- Quasi-real-time operation, i.e., ability to measure impulse responses or transfer functions in all directions within the stationarity time of the channel (the time during which the directions of important scatterers, and runlength of the signals to/from those scatterers, do not change significantly).
- Cost within the limited budget: while recently measurements (done independent of, and in parallel, to our measurements have been performed with switched arrays by AT&T [11], the cost of this sounder was much larger than the total budget available in this project.

Designing, building, and testing a sounder that fulfills all of the above requirements was thus a large and vital part of this project. In the following subsections, we will be describing the design of the different parts in the sounder. The fundamental principle is based on a SISO (single-input - single-output) transmitting into a narrow cone (directional range), whose center angle is changed with a very fast mechanical rotation.

2.1 Transmitter chain

To be able to sound the channel accurately, we employ a custom-designed Orthogonal Frequency Division Multiplexing (OFDM)-like multi-tone sequence, similar to the Zadoff-Chu sequences used in LTE, but with modifications that reduce the PAPR of filtered and oversampled signals. The bandwidth of our sounding signal is 200 MHz, constituted from 2500 subcarriers, leading to 80 kHz subcarrier spacing, corresponding to maximum 3.75 km propagation distance that can be unambiguously determined; this is anticipated to be more than enough for all the measured scenarios. Distance resolution, corresponding to the 200 MHz bandwidth, is 1.5 m.

This sounding waveform is shifted digitally to passband; in other words, we consider a digital implementation that covers the frequency range from 200-400 MHz. This waveform is loaded onto an Arbitrary Waveform Generator (AWG) prior to measurements, and is triggered once by the 1pps signal generated from a GPS-disciplined clock, then keeps on repeating indefinitely. A single repetition of this waveform is of 2 μs duration.

The AWG output is then fed into a first-stage mixing, upconverting the signal to a center frequency of 3.7 GHz, with the lower sideband occupying the 3.3-3.5 GHz range, and upper sideband occupying the 3.9-4.1 GHz range. We then filter out the upper sideband of the sounding waveform, leaving only the lower sideband, to be fed into the second mixing stage, upconverting it to the designated RF band. We resorted to such a double-mixing design in order to accurately filter out one of the side bands before going into the RF stage,

Figure 1: Frequency Response of the Sounding Waveform

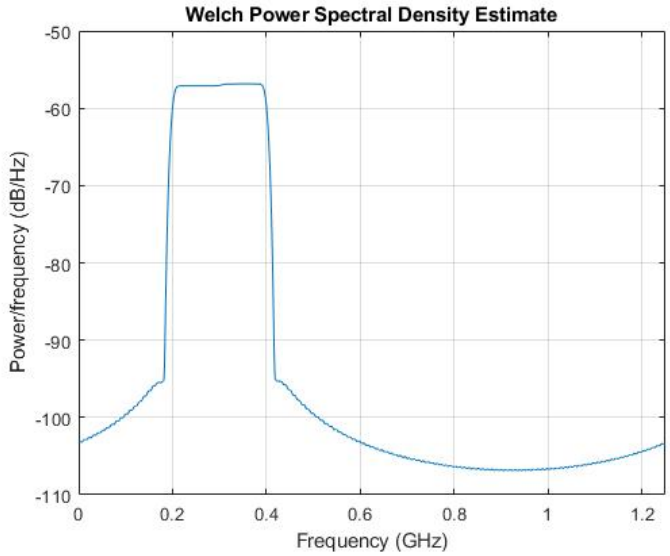

Figure 2: Transmitter RF Chain

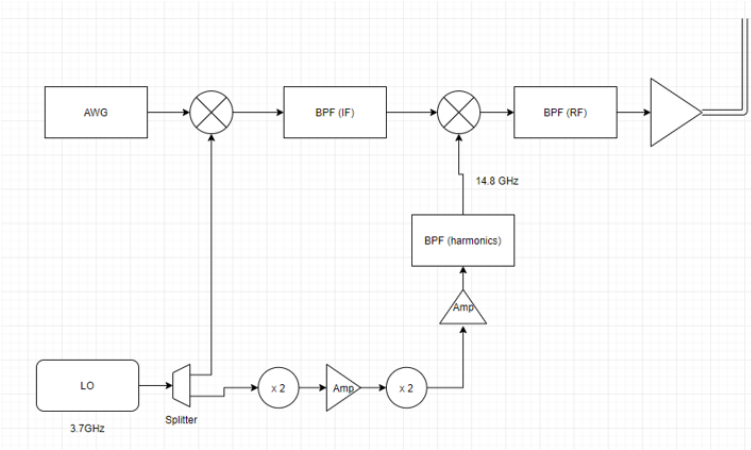

where filtering becomes a much more expensive process because of the high Q-factor filters needed at such a higher frequency.

At the RF stage, we first feed the signal into a power amplifier, increasing the power to 22 dBm, which is then radiated by the transmitter antenna. The antenna that we used for our setup was a conical horn antenna, with a beamwidth of 25 degrees.

The Local Oscillator (LO) signal used at each of the two mixing stages is generated from a 3.7 GHz reference signal. This output is then split into 2 outputs, ones of them directly upconverting the signal into the first mixing stage, while the other output passes through a series of frequency multipliers, amplifiers, and filters, to get finally to the desired frequency of 14.8 GHz. The components in this LO chain are shown in the table

Figure 3: Receiver RF Chain

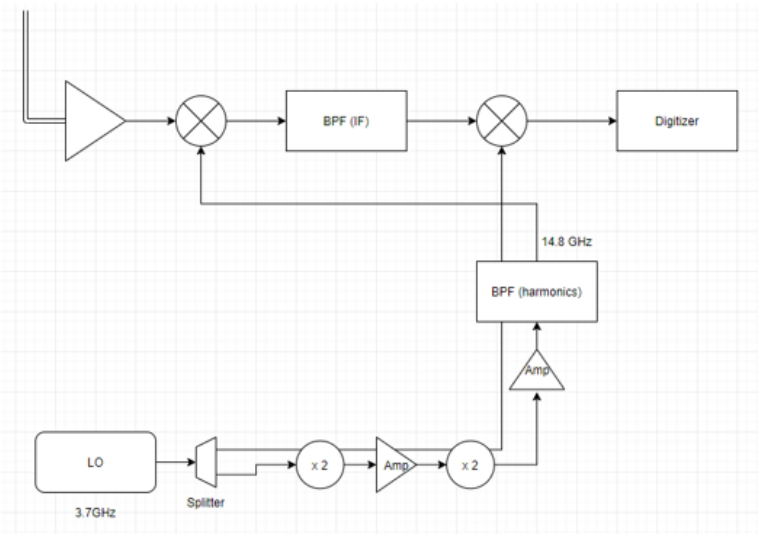

below. The mixer system on the second stage has an embedded quadrupler, taking this LO from 14.8 GHz to 59.2 GHz. The components we used are listed in the Tab. 1.

Table 1: Components List

Component	ID	Vendor
Frequency multiplier	ZX90-2-50-S+	Minicircuits
Frequency multiplier	ZX90-2-24-S+	Minicircuits
Power amplifier	ZX60-06183LN+	Minicircuits
Band pass Filter	PE87FL1005	PasterNack

2.2 Receiver chain

On the Rx side, the signal is captured using a conical horn antenna with 9 degrees beamwidth. The signal goes then into a low-noise amplifier, boosting up the power before going into the same stages as on the Tx, but in opposite direction. After the 2 mixing stages, the output is then fed into a PXIe-5162 digitizer, to capture the signal and store it for later post-processing.

The timing for the capture of the signal is obtained using the GPS-disciplined 10 MHz and 1pps signals. The capture is first triggered by the 1pps signal at the very start, allowing a synchronization between the AWG transmission and the digitizer reception, within the accuracy of the 1pps signal. After this 1pps trigger, another trigger takes over the responsibility for the process of sampling, with a period of 200 μs. This trigger is originated from the 10MHz signal, keeping the correct synchronization between the Tx and the Rx. The trigger period is designed to allow a digitizer capture of the receive signal whenever the receive direction has rotated by a half-beamwidth of the antenna.

Figure 4: Different Triggers Used for the Capture

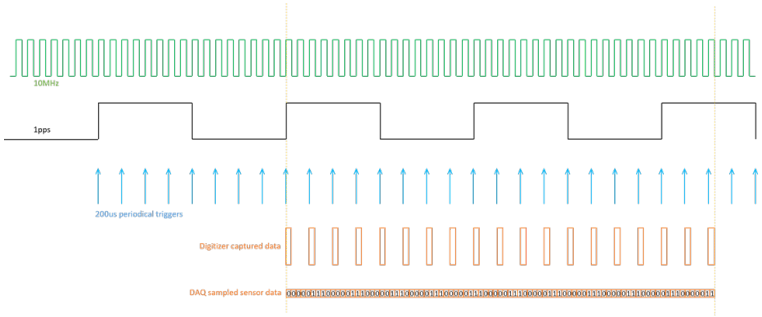

With every capture from the digitizer, we save 2 timestamps:

1. Hardware timestamp from the digitizer to synchronize between the digitizer and the angular encoding,
2. GPS-based timestamp to synchronize between the capture and the geographical location of the car on which the system is installed.

The captured data is directly streamed into an external RAID array with no real-time processing, to avoid any possible induced latencies. The streamed file is usually of a very large size, so we implemented a python program that goes over the measurement file and divides in into chunks of 2 seconds each. This data, in addition to the generated timestamps, is then matched with the sensor angular encoding data, giving a channel transfer function for every angular direction, and allowing to build the full MIMO (multiple-input multiple-output) snapshot.

2.3 Mechanical structure

The mechanical structure of our system is based on 2 main components: a fixed object (FO) and a moving/rotating object (MO). The goal from this setup is to allow our sounder to automatically scan the full 360-degree azimuth plane, in a short period of time, and without any needed human intervention/adjustment. To achieve this goal of scanning the channel using mechanically rotating beams, we need to carefully choose our components, including the antenna, the angular encoder, and the full rotating structure, making sure that we are able to match every beam direction with a specific angular orientation, allowing us to build this "virtual array" structure. The Tx-based MO rotates at a speed of 80-100 RPM, while the Rx-based MO rotates at a speed of 3000 to 3400 RPM, allowing us to get a full MIMO snapshot every 0.6-0.8 s.

To measure the correct angular orientation $(\phi_{0,\mathrm{Tx}}(t), \phi_{0,\mathrm{Rx}}(t))$ at any time, we designed and built an optical photoelectric sensor system, with a polarized reflecting tape attached to the MO, and the sensor mounted on top of the FO. We have used a polarized tape due to their much higher resilience to ambient daylight. The polarized tape was also cut into a very specific coded pattern that can be directly recognized in the captured data, allowing a 1-to-1 mapping between the sensor data and the actual physical orientation. The

Figure 5: Calibration Measurement inside the Anechoic Chamber

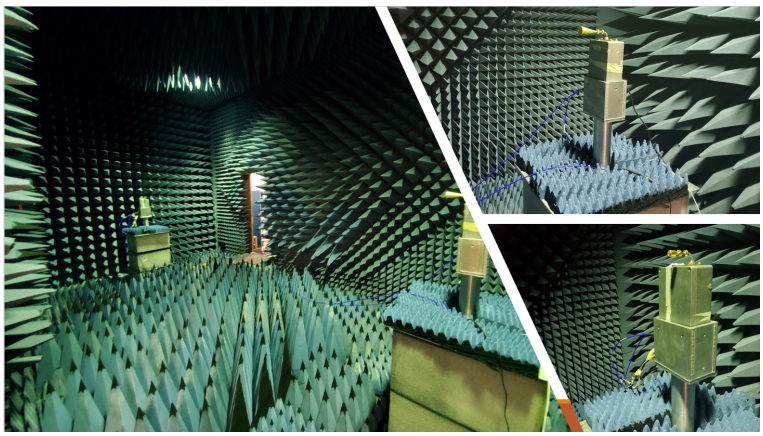

sensor data is captured using a NI DAQ board with different sampling rate at two sides for their different rotation speed. The sample rate of the Tx is 120 KS/s (kilo samples per second) and the rate for the Rx is 2.5 MS/s. This high sampling rate allows us to capture the sensor reflections with time resolution of 8.3 μs and 0.4 μs, which is more than enough to accurately represent the captured data from the reflective tapes on both sides. With every capture of the data, corresponding to 50 KS, we save a GPS-based timestamp. The data, with the corresponding timestamps, are processed and matched with the channel-measurement data, giving a channel transfer function in every direction.

2.4 Calibration

Channel sounder calibration consists of two main steps: (i) back-to-back calibration, and (ii) array calibration. The former measures the frequency selectivity and other distortions of the sounding equipment; the latter measures the characteristics of the antennas.

This implies that array calibration is important for any quality model extraction. The characterization of the response of the antenna, including the supporting mechanical structure, at every angular rotating position (thus the response of the full virtual array) has to be therefore measured in an anechoic chamber. We performed such a calibration in our anechoic chamber at USC, see Fig. 5.

As for the back-to-back calibration of our system, conventionally it is performed using a cable connection between the Tx and the Rx, adding attenuators to protect the receiver end. However, given the high sensitivity to motion of the cables at our considered high operating frequency, we resorted to a reference small-distance measurement as our back-to-back calibration. Therefore, before doing any of our measurement scenarios, the cars were positioned bumper-to-bumper and a reference measurement was performed. This reference distance measurement was done as a continuous streaming measurement, allowing us to capture the waveform over multiple repetitions and therefore averaging over multiple realization of the reference channel

to further improve the Signal-to-Noise Ratio (SNR) of the system calibration data, i.e.

$$\mathrm{Y}_{\mathrm{REF}}(f) = \mathbb{E}[\mathrm{Y}(f)]$$

where $\mathrm{Y}_{\mathrm{REF}}(f)$ is our final system calibration result. This system response is then used for the pre-processing of the measurement data that calculated by equation (1)

$$\mathrm{H}(f) = \frac{\mathrm{Y}_{\mathrm{MEAS}}(f)}{\mathrm{Y}_{\mathrm{REF}}(f)} \tag{1}$$

where $\mathrm{H}(f)$ is the channel transfer function, and $\mathrm{Y}_{\mathrm{MEAS}}(f)$ is the frequency transform of the captured measurement data. Note that this back-to-back measurement inherently includes the properties of the transmit and receive antennas; since those frequency characteristics are already known from the measurement in the anechoic chamber, they can (if necessary) be eliminated from the back-to-back measurements.

3 Parameter Extraction

3.1 What we measure

As described in the previous sections, the goal from this work is to measure and model the double-directional channel between the Transmitter and the Receiver. The time-varying complex impulse response of the propagation channel can be modeled as the superposition of N paths at the Rx side, i.e.

$$\mathrm{h}(t,\tau,\phi_{\mathrm{R}},\phi_{\mathrm{T}}) = \sum_{l=1}^{N} \alpha_l e^{j\gamma_l t}\delta(\tau-\tau_l)\delta(\phi_{\mathrm{R}}-\phi_{\mathrm{R},l})\delta(\phi_{\mathrm{T}}-\phi_{\mathrm{T},l})\mathbf{b}_{\mathrm{R}}(\phi_{\mathrm{R},l})\mathbf{b}_{\mathrm{T}}(\phi_{\mathrm{T},l}) \tag{2}$$

where $a_l, \gamma_l, \tau_l, \phi_{R,l}$ and $\phi_{T,l}$ are the gain, Doppler shift, propagation delay, direction-of-departure (DoD) and direction-of-arrival (DoA) of the l^{th} path, respectively. $\mathbf{b}_{\mathrm{T}}(\phi_{\mathrm{T},l})$ and $\mathbf{b}_{\mathrm{R}}(\phi_{\mathrm{R},l})$ are the contributions of the Tx and Rx (complex amplitude) antenna radiation patterns in the directions of $\phi_{T,l}$ and $\phi_{R,l}$ respectively. Note that in this model, we are assuming that the radio wave propagation occurs only in the horizontal plane, i.e. elevation will not be considered.[1]

What we actually measure is the convolution of this impulse response with the time-variant antenna patterns at the Tx and Rx. Due to the short duration of the sounding signal, the antenna pattern can be considered constant for the duration of the signal, thus the effective impulse response measured at time t can be written as equation (3):

$$\mathrm{h}(t,\tau) = \int\int \mathrm{h}(t,\tau,\phi_{\mathrm{T}},\phi_{\mathrm{R}})\mathbf{b}_{\mathrm{T}}(\phi_{\mathrm{T}}-\omega_{\mathrm{T}}t)\mathbf{b}_{\mathrm{R}}(\phi_{\mathrm{R}}-\omega_{\mathrm{R}}t)d\phi_{\mathrm{T}}d\phi_{\mathrm{R}} \tag{3}$$

where ω_{T} and ω_{r} are the rotation speeds of the Tx and Rx horns respectively.

The received signal can also be expressed similarly as equation (4)

$$r(t) = \int\int\int \mathrm{h}(t,\tau,\phi_{\mathrm{T}},\phi_{\mathrm{R}})w(t-\tau)\mathbf{b}_{\mathrm{T}}(\phi_{\mathrm{T}}-\omega_{\mathrm{T}}t)\mathbf{b}_{\mathrm{R}}(\phi_{\mathrm{R}}-\omega_{\mathrm{R}}t)d\tau d\phi_{\mathrm{T}}d\phi_{\mathrm{R}} \tag{4}$$

where $w(t)$ is the system (back-to-back) impulse response.

Given all of the above, the actually measured samples of the channel for every delay point can be organized on a diagonal-like grid, where every point on the grid corresponds to a certain $(\phi_{\mathrm{T}}(t), \phi_{\mathrm{R}}(t))$ pair. Given the continuous rotation on both ends, the grid would look as shown in figures 6a; from these results the more conventional representation on a rectangular grid, as shown in 6b, can be obtained.

[1] This is a reasonable assumption for V2V measurements, since TX and RX are at the same height; furthermore, diffraction (e.g., over a truck that blocks the LOS between TX and RX) is an inefficient process due to the high frequency at which we measure. Finally, a ground bounce that would arrive at a steep elevation angle would be shielded off by the hood and roof of the car, and thus not be relevant for antenna placement on the roof of the car.

Figure 6: Power Spectrum with A Zoomed-in Section

(a) Diagonal Grid of Measurement Positions **(b) Rectangular Interpolated Grid**

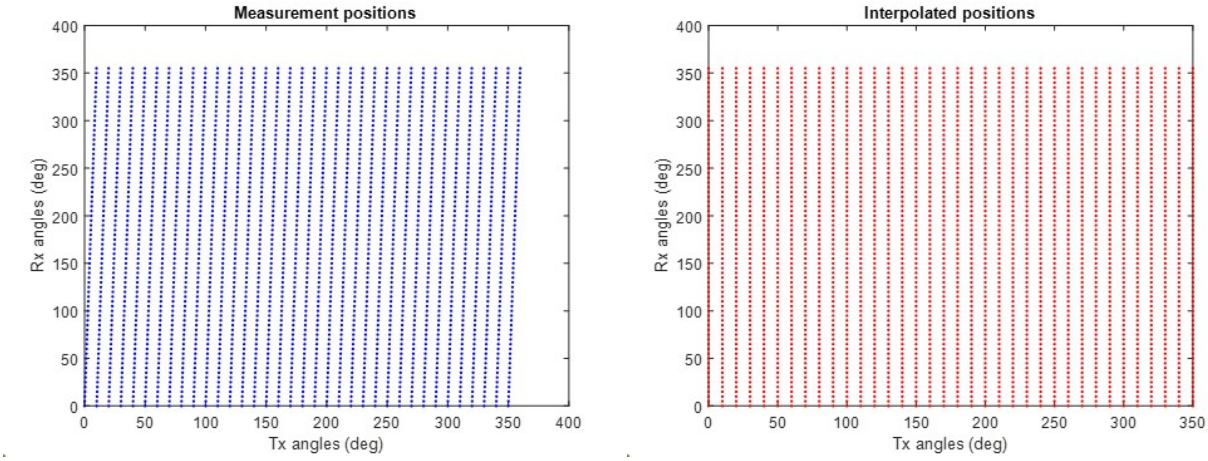

3.2 Problems encountered

During the measurement campaigns, we have faced several problems that we discovered afterwards during the data processing (the performed measurements, intended originally as proof-of-principle, were designed to discover such problems and form the basis for later corrections). However, due to the COVID-19 pandemic and the resulting restrictions on laboratory work and particular measurement campaigns that require interactions of multiple people, we have not been able to redo the measurement campaigns even within the (extended) project timeline. These problems will be summarized in this section and we will provide details on how and what we were able to salvage from the measured data. Worth noting that all these problems were solved and adjustments were made on the system in a laboratory environment to make sure we do not suffer from such issues again. We plan to repeat the measurement campaign with the improved setup and publish the results as soon as the COVID-19 situation is resolved.

The first problem relates to the sensor setup. During the measurement, because of vibrations of the cars during the driving, the sensor data on the Rx side were lost. That means that no direct indication is available on where the zero-angle is, i.e. the angle where the Tx and the Rx are in direct LoS. To tackle that issue, we resorted to manually observing the received power vs time plot, detecting the time instant of the LoS (i.e., the highest power), and mapping it into an angular direction. In addition, although we did not lose the sensor data on the Tx side, the sensor was detecting some false positives, showing double pulses where a single pulse should exist. Fortunately, a quick pre-processing MATLAB code was able to detect such abnormal double-pulses and remove them, allowing us to generate a "clean" sensor data on the Tx side. The figures are shown in Fig. 7.

Figure 7: Before and After the Sensor Fake Pulses Smoothing

(a) Before Sensor Data Smoothing

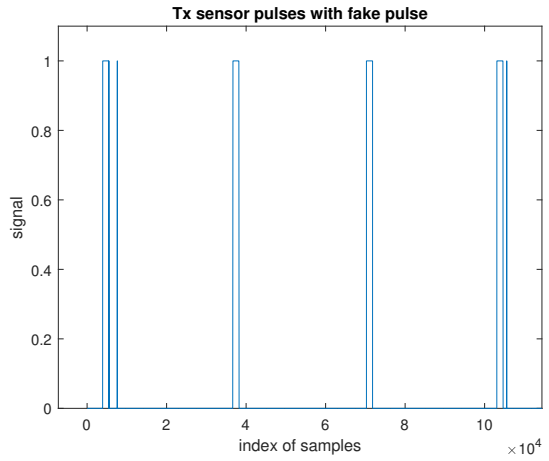

(b) After Sensor Data Smoothing

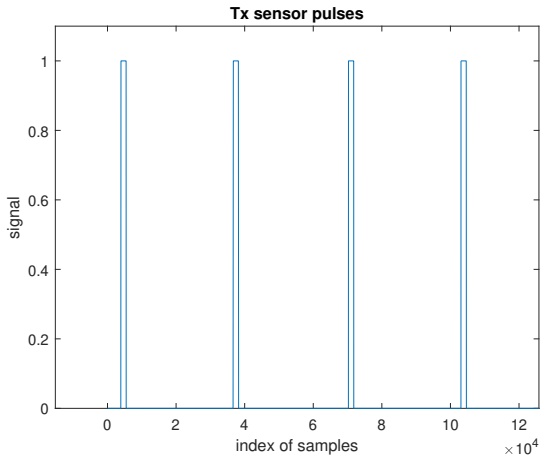

Although it is difficult to get an accurate estimation of the speed of the Rx rotation because of the missing sensor data, we resorted into observing the Power vs Time plot in the LoS direction, and checking how much time is spent in between 2 power peaks. In addition, we also used this plot to know how many Rx positions we have captured during a full rotation, deciding the dimension of this specific SIMO (single-input multiple-output) capture like the Fig. 8 shows. Due to the momentum of the rotation, it is reasonable to expect that the rotation speed does not change significantly during one full rotation.

Further problems arose in the sounder design, due to the NI digitizer not being able to capture multiple records in a synced fashion (it needs to go into a software routine before switching into another capture). This introduces a software random delay into the captures. Consequently, whenever we stop the capture at a certain direction and move to the next one, there is a random delay introduced in between. This random delay makes it impossible to extract the relative delay information between different horn orientations, and consequently a reconstruction of the omni-directional power delay profile from the set of directional measurements is not possible (note that [31] faced similar problems; in that case if was possible to regain synchronization between horn orientations through comparison of measurement data with ray tracing; in our case this approach is not feasible due to the dynamic measurement environment and the absence of detailed-enough maps of the environment that would include, e.g., parked cars and similar objects).

However, we can still extract information about the directional power delay profile, that is the power delay profile in the beam combination that would provide maximum total received power (and is thus most likely to be used in a practical V2V communication system). It is actually this directional PDP that is necessary for the design of V2V operating parameters such as equalizer length or cyclic prefix.

Figure 8: Power Plot Used to Estimate Rx Speed And Number of Rx Positions per Tx Position

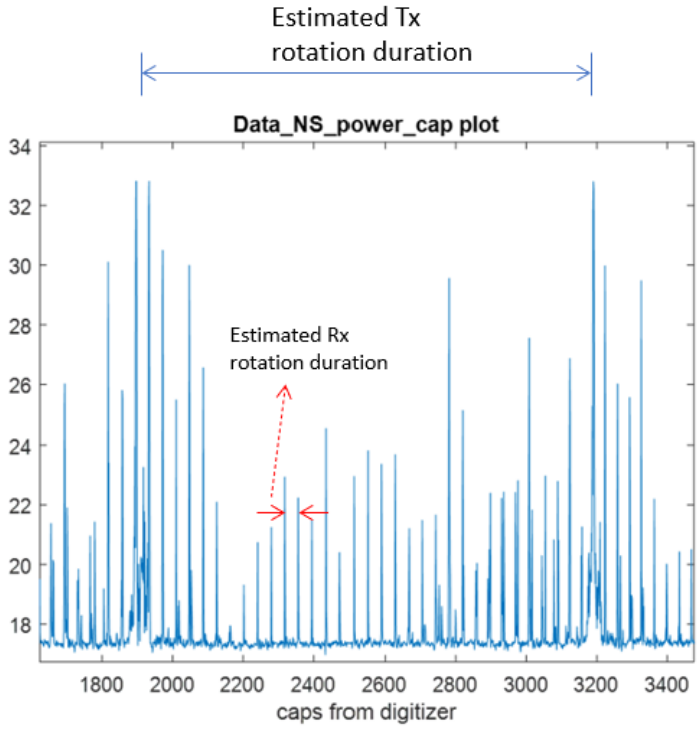

Expressing these inaccuracies of the triggering, the sampling, and the random introduced delay into mathematical formulation, we see that the triggering period has a mean of 510 μs with error of +/- 130 μs. This translates into an average angle difference of 10.4° on the Rx, with error +/- 2.65°. Having such an angular step on the Rx means that we get 34 capturing positions, corresponding to the number of Rx antennas in the MIMO snapshot. Furthermore, we see that the inaccuracy of the angle orientation for a given sampling time is considerably lower than the half-beamwidth of the Tx and RX. Thus, the mapping from the (time-stamped) measurement samples to a particular direction is not affected.

3.3 Measurement Data Processing

In order to describe and model the channel as mentioned in the previous sections, we capture and store the following datasets to aid us in our processing:

- ADC captured data and associated timestamp
- Rx sensor data and timestamp
- Tx sensor data and timestamp
- GPS timestamp that associated with video recording

While the main data corresponding to the channel transfer function is captured in the first item, we use

Figure 9: Power Spectrum without Cutout at LoS Direction with A Zoomed-in Section

(a) Power Spectrum without Cut out at LoS

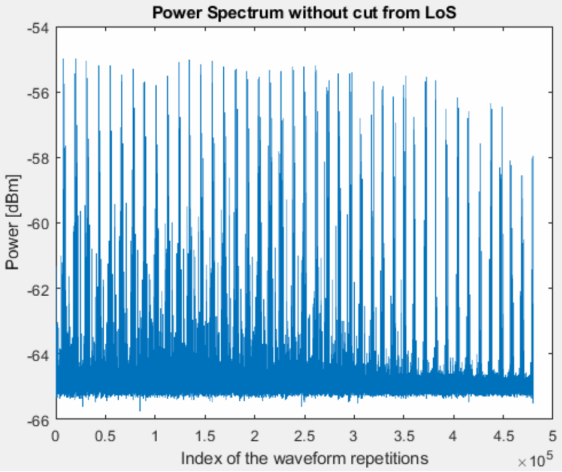

(b) Zoomed-in Power Spectrum without Cutout at LoS

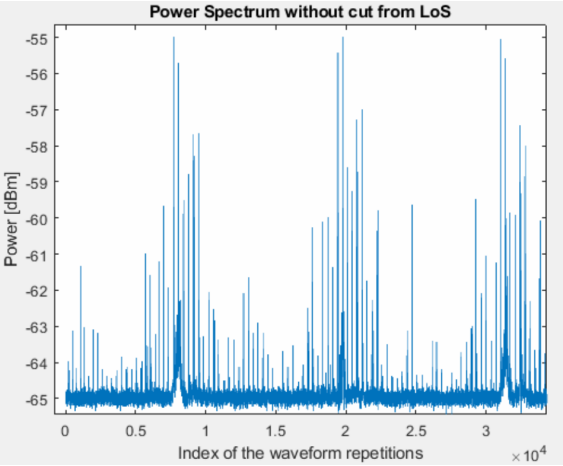

the different sensor data and timestamps as a reference, to know how to match every ADC capture with a corresponding angular direction.

3.3.1 MIMO snapshot

Peak and pulse detection As a first processing step, we need to reshape the captured stream of data into a form that is more meaningful to our processing. This is done by re-arranging the raw data vector into a matrix of dimension $N_r \times N_{sr}$, where N_r is the total number of repetitions, and N_{sr} is the number of samples per capture.

$$\mathbf{A} \in \mathbb{R}^{N_d \times 1} \quad \Rightarrow \quad \mathbf{A} \in \mathbb{R}^{N_r \times N_{sr}} \tag{5}$$

where N_d is the number of data points in the initial data stream vector and N_{sr} is the number of each repetition. In our measurement, $N_{sr} = 2500$, which means there are 2500 samples in each waveform repetition burst.

Because of the mechanical issue mentioned in the section 3.2, we do not have the sensor data at the Rx side, which means we cannot map the data directly onto a particular direction by using the sensor information. Alternatively, we choose to use the power spectrum (PS) in time domain to help us to determine the directions of the data. The PS we need to use is the power of repetitions versus time, so the first step we need to process is to generate the power of each waveform repetition by using equation (6)

$$\mathrm{P}_{\mathrm{A}n} = 10\log_{10}\left(\sum_{\mathrm{j}} |\mathbf{A}_{n,\mathrm{j}}|^2\right), \ \mathrm{j} = 1, 2, ..., 2500 \tag{6}$$

Figure 10: Power Spectrum with A Zoomed-in Section

(a) Power Spectrum

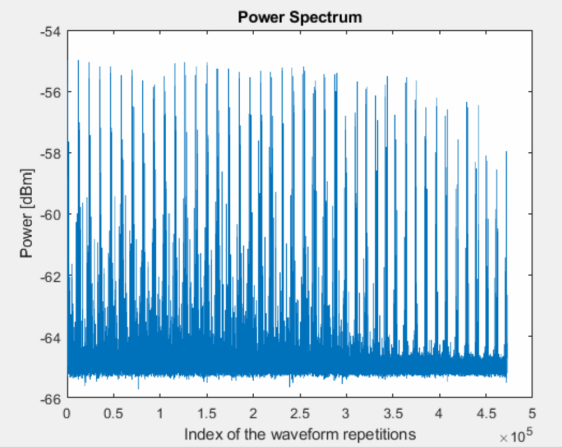

(b) Zoomed-in Power Spectrum

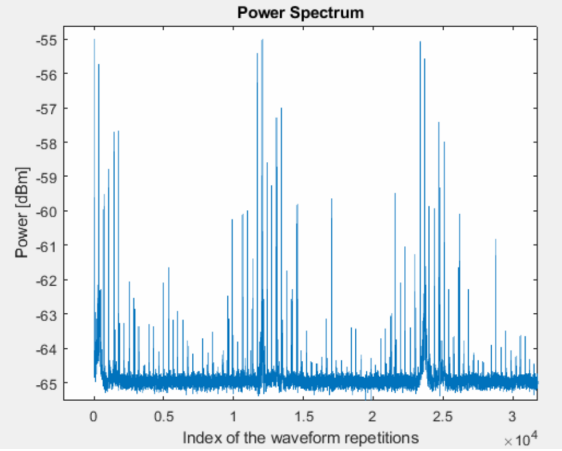

where n represents the index of the waveform repetitions. So $\mathbf{P}_{\mathrm{A}}$ is a vector and $\mathbf{P}_{\mathrm{A}} \in \mathbb{R}^{N_r \times 1}$.

Now we can easily plot the PS by using $\mathbf{P}_{\mathrm{A}}$, which is shown by Fig. 9a. We can see from Fig. 9b that there are few big peaks and many small pulses in the PS. Since the RPM of the object at the Rx side is much faster than the one on the Tx side, and the PS in Fig. 9 belongs to a scenario where a LoS path exists, we can conclude that the big peaks represent the moments that the Tx is facing at the Rx after completing a full Tx rotation and the small pulses represent the moments when the Rx is orientated towards the Tx after performing a full Rx rotation. This pattern can be used as criterion to distinguish different MIMO snapshots. Given the very-low probability of starting the capture at the instant when the Tx and the Rx are directly facing each others, it is very likely that the data starts somewhere with low power. To unify the starting moment of the capture across all of our evaluations, we discard all the data before the first high peak (signifying the start of the first MIMO snapshot) generating a PS like the one in Fig. 10, and all the processing afterwards will be based on the PS that starts at LoS direction.

MIMO snapshots indexing We design a peak detection algorithm to automatically find the peaks and pulses from the PS. The algorithm uses the similarities between the different MIMO snapshots in terms of power and trend of peaks in order to get a more accurate estimate of the start and end points of each MIMO snapshot. For example, Fig. 10b shows the first 2 MIMO snapshots of the scenario and there are three peaks. The algorithm uses the similarities between the different snapshots to know which peak it should take as the LoS peak, i.e. the peak at which a new MIMO snapshot will start. Besides, we also use the sensor data at the Tx side to help improve the accuracy. The sensor information from the Tx side offers a reference about how fast the Tx is from last peak to the current peak, which can be used as a sanity check to ensure that the MIMO snapshots ends at the right place.

After the peak detection, we know the capture indices within every MIMO snapshot. As a result, we save these indices into vectors, so they can be called whenever we need to access the data of any snapshot in the later processing steps.

3.3.2 Averaging and power thresholding

We then start processing the data matrix $\mathbf{A}$ over multiple steps. We reshape $\mathbf{A}$ again, from $\mathbf{A} \in \mathbb{R}^{N_r \times N_{sr}}$ to $\mathbf{A} \in \mathbb{R}^{N_c \times N_{sc}}$, where N_c is the number of captures, and N_{sc} is the number of samples per capture. In our case, N_{sc} is 20000, corresponding to 8 repetitions of our 2500-samples waveform. Then, we transform $\mathbf{A}$ into the frequency domain, where we are averaging over the 8 repetitions of the waveform to average out the white noise and boost our SNR:

$$\mathbf{A}_{\mathrm{i},\ell}(f_k) = \mathcal{F}[\mathbf{A}_{\mathrm{i},\ell}(t_j)] \tag{7}$$

$$\mathbf{A}'_{\mathrm{i}}(f_k) = \mathbb{E}[\mathbf{A}_{\mathrm{i}}(f_k)] = \overline{\sum_{\ell} \mathbf{A}_{\mathrm{i},\ell}(f_k)}, \tag{8}$$

where $\mathrm{i} = 1, 2, ...N_c$ and $\ell = 1, 2, ..., 7, 8$. In equation (7) and (8), i is the index of the capture and ℓ represents the index of the repetition within the same capture. t_j and f_k are the discrete variables for time and frequency in their associated domains.

After the averaging operation, we call the new averaged data matrix $\mathbf{A}'$ where $\mathbf{A}' \in \mathbb{C}^{N_c \times 2500}$, each row corresponding to an averaged capture: $\mathbf{A}'_i \in \mathbb{C}^{1 \times 2500}$. This matrix of the received data is what we can use as explained in the Calibration section, to generate the corresponding calibrated channel transfer function $\mathbf{H}_{\mathrm{i}}(f_k)$ and thereafter the channel impulse response $\mathbf{h}_{\mathrm{i}}(t_j)$, where

$$\mathbf{h}_{\mathrm{i}}(t_j) = \mathcal{F}^{-1}[\mathbf{H}_{\mathrm{i}}(f_k)], \text{ where } \mathbf{h} \in \mathbb{C}^{N_c \times 401} \tag{9}$$

where 401 is the number of samples in the delay range of interest (up to 300 m).

At this moment, we have the vectors that are storing the indices of the captures for each MIMO snapshot from section 3.3.1, and we have the CIRs matrix $\mathbf{h}$. We can access any snapshot by calling the corresponding vector along the first dimension (row dimension), thus accessing the CIRs from $\mathbf{h}$ mapping to every MIMO snapshot.

Then for every MIMO snapshot, we will use noise-thresholding to the snapshot as a whole, i.e. we will determine a noise threshold to process every capture within the same snapshot. To do that, we need to find the peak power and the noise power of the snapshot. Fig. 11 shows two threshold levels: threshold 1 and

Figure 11: CIR Noise-threshold Cut off Levels Assuming 8 dB Below Max Power and 10 dB above Noise Level

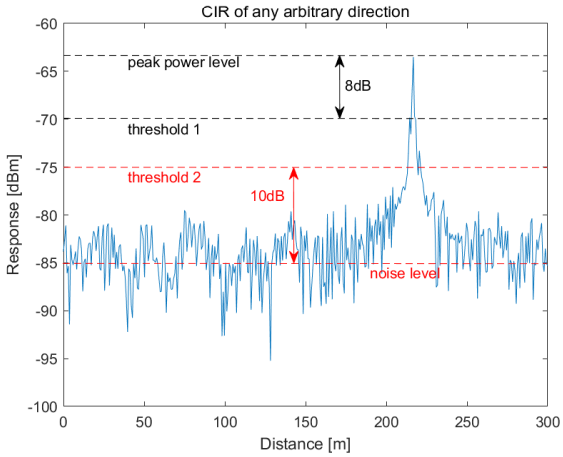

threshold 2, defined as follows:

$$\text{threshold}_1 = \text{maximum power of the snapshot} - 15 \text{ dB} \tag{10}$$

$$\text{threshold}_2 = \text{noise level of the snapshot} + 10 \text{ dB} \tag{11}$$

The cut off level will be determined by $\max(\text{threshold}_1, \text{threshold}_2)$. The two threshold levels are motivated as follows: firstly, we eliminate all contributions that are more than 15 dB below the maximum received power; this can be justified by the fact that at mmWave frequencies, lower-order modulation formats will be used, which do not require a large SINR for proper operation. More importantly, removing those weaker components reduces the risk of including spurious components that are weak, but might have a disproportionate effect on the delay and angular spreads. Furthermore, we eliminate all components within a certain range of the noise level, to reduce the probability that a noise peak is mistaken for a multipath component. While some investigations in the literature use lower treshold levels (e.g., 6 dB above noise level), we use here a more conservative value; this turns out to have little impact on the overall results, since in almost all cases threshold_1 is the dominant factor.

For the CIR from a particular direction, all the values that below the cut off level will be set to a very small value, such as -300dBm, which eliminates their impact on the total CIR power. We denote the updated CIR as $\mathbf{h'}_{\mathrm{i}}(t_j)$. After updating the CIR from every direction over the measurement, the updated power delay profile can be obtained from equation (12), and the total received power by equation (13).

$$\mathbf{p}_{\mathrm{h_i}}(\tau) = \sum_{t_j} |\mathbf{h'}_{\mathrm{i}}(t_j, \tau)|^2 \tag{12}$$

$$\mathbf{P}_{\mathrm{h_i}} = \sum_{\tau} \mathbf{p}_{\mathrm{h_i}}(\tau) \tag{13}$$

where $\mathbf{p}_{\mathrm{h}} \in \mathbb{R}^{N_c \times 401}$ and $\mathbf{P}_{\mathrm{h}} \in \mathbb{R}^{N_c \times 1}$. $\mathbf{P}_{\mathrm{h}}$ is the updated power of the CIR vector for every averaged capture (every SNR-boosted sample position/direction).

Similarly, we are able to use the vectors that saving the capture indices of each MIMO snapshot to find the corresponding $\mathbf{P}_{\mathrm{h}}$, so that we have the updated CIR power vector for each MIMO snapshot, denoted as $\mathbf{P}_{\mathrm{MIMO}}$. The lengths of the updated CIR power vectors can be different concerning different snapshots. But that is not a problem for our measurements as long as enough positions are being taken per rotation, and as long as we have a measure of how many positions exist per MIMO snapshot.

3.3.3 Mapping data into APSs

In order to map a MIMO snapshot into the angular domain, and thus generate the corresponding APS, we need first to determine the number of Rx rotations in it, which can be denoted by $\mathbf{N}_{\mathrm{DoD}}(m)$, where m is the index of the MIMO snapshot. This number corresponds to the number of captured Tx positions, since we do a full Rx rotation for every Tx position. We also can determine the number of captures within every Rx rotation, denoted by $\mathbf{N}_{\mathrm{DOA}}(m, k)$, where m is the order of MIMO snapshots and k is the index of the Rx rotations in the m^{th} snapshot.

Having generated the map of measured angles on both the Tx and the Rx sides, we can now assign a power value per angular pair, according to the indices and the number of positions in that snapshot.

Here, we distinguish between 3 kinds of APSs, as shown in Fig. 12. The first APS, shown in the leftmost figure, is the APS directly generated from the raw data. Although it reflects the power distribution in the angular domain, a lot of what we are visualizing is due to noise, since the dynamic range of our system (without post-processing, i.e., without exploitation of sparsity in the delay domain) is on the order of 20 dB. Therefore, the plot in the center is what the APS looks like after noise thresholding, which is the technique described in the section 3.3.2. Although this is a cleaner APS, it still suffers from the problem of having a vertical and a horizontal lines, going through the center, namely the lines DoD = 0 and DoA = 0. We conjecture that these lines are due to the leakage of the rotating unit, in addition to the reflections caused by the system when mounted on the vehicles. The third plot (plot on the right) is what the APS would look like, after eliminating those 2 effects, leaving us with a much cleaner APS that is a reflection of the measured channel. In particular, we eliminate components with DoD=0, and DoA $\neq$ 0, as well as DoA=0 and DoD $\neq$ 0. We stress that these are ad-hoc modifications, and in the future will be replaced by a hardware design with reduced leakage. The ad-hoc postprocessing is motivated by the fact that physical processes that transmit directly towards the RX, but arrive from a different direction, would require at

Figure 12: Wall: Raw APS, APS with Noise Thresholding, and APS with Calibration

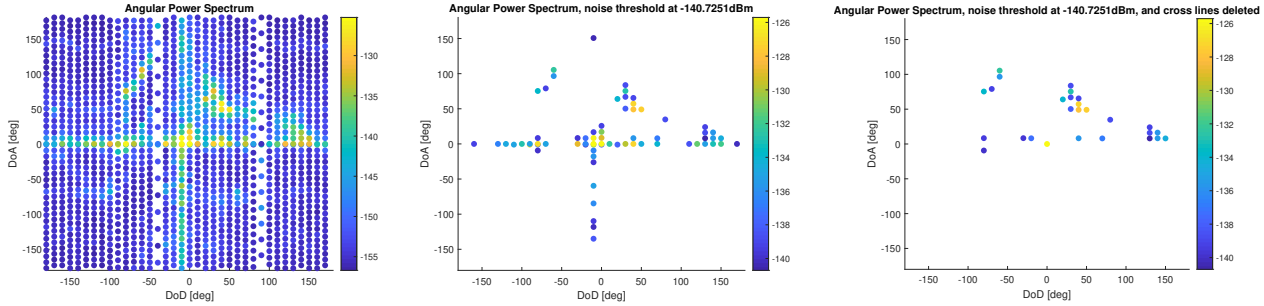

least double-scattering, which is expected to make only extremely weak contributions. The only exception might be components that are transmitted into DoD = 0°, and arrive at DoA = 180°, i.e., components that are transmitted towards the Rx, get reflected by an object (car, truck) in the same lane, and from there to the Rx at DoA = 180°, using only a single reflection; or vice versa with DoA = 0°, and arrive at DoD = 180°. However, this process could not occur in our measurements because no cars were (within reasonable proximity) in front of/behind our TX and RX cars. **Thus, in the evaluations section of this report, we will only provide the last version of the APSs, i.e. the APS after noise thresholding and after eliminating the mechanical-structure effect.**.

3.3.4 Delay and angular spreads

For the RMS delay and angular spreads calculation, we will be using the adjusted APSs as explained in section 3.3.3.

To calculate the RMS delay spread, we start out by computing the zeroth-order moment -i.e., *time-integrated power* by using equation (14):

$$P_{\mathrm{m}} = \int_{-\infty}^{\infty} P_{\mathrm{h}}(\tau) d\tau \tag{14}$$

The normalized first-order moment, the *mean delay*, is given by equation (15):

$$T_{\mathrm{m}} = \frac{\int_{-\infty}^{\infty} P_{\mathrm{h}}(\tau)\tau d\tau}{P_{\mathrm{m}}} \tag{15}$$

The normalized second-order central moment, which is known as *rms delay spread* and is defined by equation (16)

$$S_{\tau} = \sqrt{\frac{\int_{-\infty}^{\infty} P_{\mathrm{h}}(\tau)\tau^2 d\tau}{P_{\mathrm{m}}} - T_{\mathrm{m}}^2} \tag{16}$$

As for the angular spreads, There are two forms of angular spread calculation.

$$S_\phi = \sqrt{\frac{\int APS(\phi)\phi^2 d\phi}{\int APS(\phi)d\phi} - \left(\frac{\int APS(\phi)\phi d\phi}{\int APS(\phi)d\phi}\right)^2} \tag{17}$$

Equation (17) has unit in radians or degrees, depending on the unit of ϕ. However, there is another form of angular spread, which better handles the periodic nature of the angular spectrum (i.e., the fact that two components at 5 and 15 degrees should result in the same angular spread as two components at 5 and 355 degree). This definition, first suggested by Fleury [12], is computed as:

$$S_\phi = \sqrt{\frac{\int |\exp(j\phi) - \mu_\phi|^2 APS(\phi)d\phi}{\int APS(\phi)d\phi}} \tag{18}$$

with

$$\mu_\phi = \frac{\int \exp(j\phi) APS(\phi)d\phi}{\int APS(\phi)d\phi} \tag{19}$$

4 Measurement Campaign

4.1 Measurements vehicles and setup

In order to perform a realistic characterization of the propagation channel, two pickup trucks were used at the Tx and the Rx sides during the measurements. During the first days of measurement we have used JEEP Gladiators as the trucks of choice, while we used Ford F150 trucks for the second set of days, as shown in Fig. 13.

Figure 13: Photos of the Trucks Used as Our Test Vehicles

(a) FORD F150 Pickup Truck **(b) JEEP Gladiator Pickup Truck**

Figure 14: Photos of the System Mounted on the Trucks

(a) System Mount - Side View **(b) System Mount - Back View**

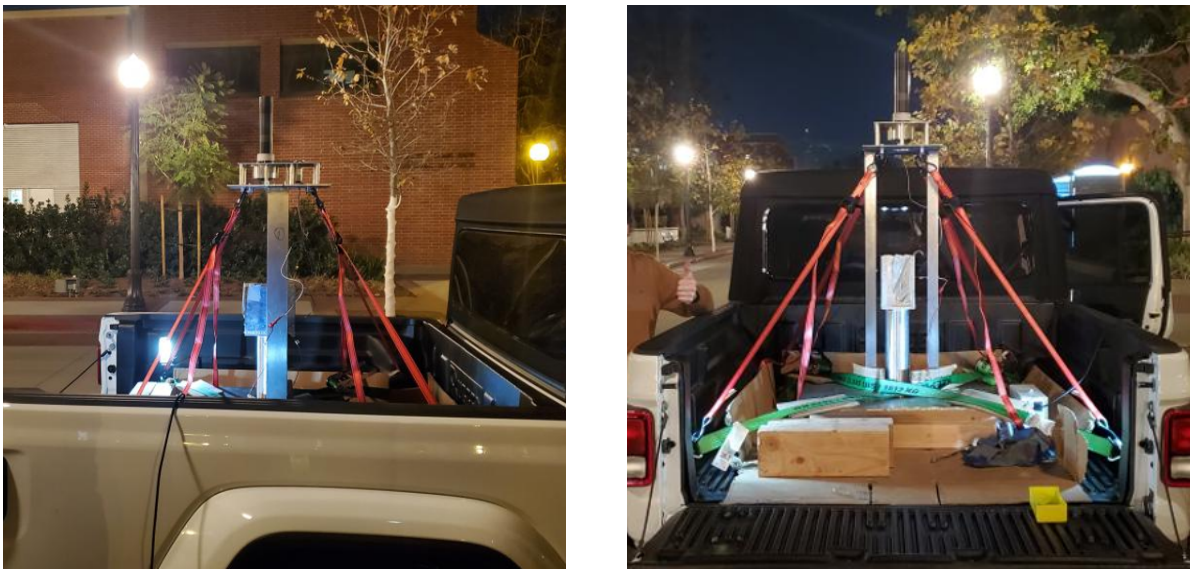

These trucks were chosen based on height, width, and bed size. The sounder system and the needed batteries

for power supply were loaded on the bed and on the passenger seats in a way to make sure that it is well positioned and solid, able to withstand vibrations and driving at higher speeds, as shown in the figures. The connection between the equipment on the bed and inside the vehicles were done through RF cables running through the back window of the truck. Fig. 14 shows the side and back view of the mounted sounding system.

4.2 Measurement environments

In this section, we will describe the different environments that were measured, providing pictures and map views, before we go into the detailed evaluation of every measurement scenario in the next section.

4.2.1 Driving next to a wall

This scenario was done to observe the effect of a typical building wall, as frequently occurring in urban street canyons, on our channel and propagation characteristics. The route taken for the measurement can be seen in Fig. 15a, where we mark in red cross the starting position, and in blue cross the ending position. A street-view photo of the environment capturing the wall is shown in Fig. 15b. The reflective wall in this scenario was the Ronald Tutor Hall (RTH) building.The Tx stays in a fixed position throughout the measurement, while the Rx moves away from the Tx at a constant speed. The driving distance corresponds to around 8m.

Figure 15: Photos of the Wall Scenario

(a) Map View of the Route Taken

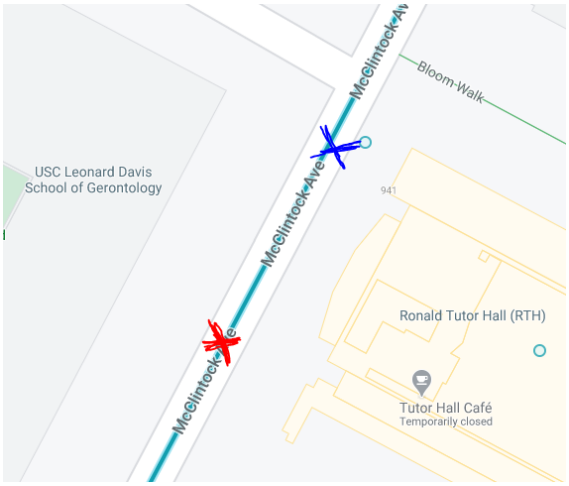

(b) Picture View of the Wall Environment

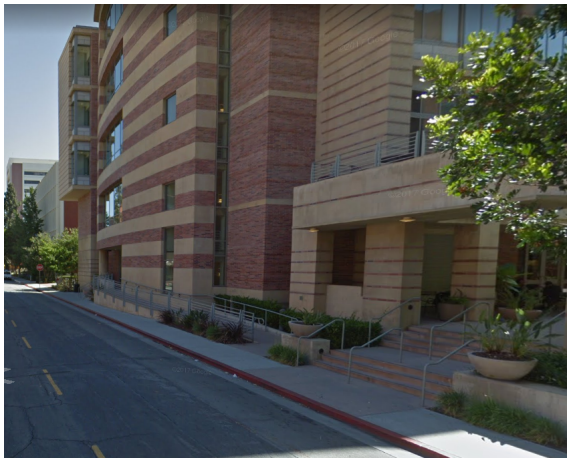

4.2.2 In front and behind a truck

In this scenario, we parked the Tx and the Rx vehicles in front and behind a truck respectively, as shown in Fig. 16. The truck serves as a blockage for the LoS, allowing multi-path components to diffract around the edges of the truck.

Figure 16: Photo of the Truck Scenario

4.2.3 Mixed traffic scenario

In this scenario, we organized a mixed truck/passenger car traffic setup as shown in Fig. 17. The scenario that was investigated in this case is the "Communication between adjacent vehicles", which is the most straightforward scenario where we model the communication between two cars that are following each other in the convoy.

Figure 17: Photos of the Traffic Scenario

5 Evaluations

In this section, we will present the evaluation results of each of the measurement scenarios described in the previous section. For every scenario, we will present the estimated RPM plots on the Tx, showing the stability of the rotatory motion with time. On the Rx side however, due to not having the sensor data as we explained in previous sections, we will not be able to provide a measure of the stability of the Rx RPM. This does not affect our evaluations however, because the Tx RPM is the one used to divide the data into MIMO snapshots, by counting the number of pulses we get in a single Tx rotation, as explained previously.

In addition to the RPM plots, we will provide directional power-delay profile, directional RMS delay spread, in the direction of the maximum power component. We will also provide sample APSs for the different MIMO snapshots, and estimate the angular spreads on both the Tx and the Rx. Finally, we will include a power-trend plot that shows how the power is changing as the measurement progresses. We will also provide possible explanations of the results. We stress that these explanations are not necessarily the true ones; we can only say that the reasons we give for certain observations are physically reasonable and in line with the observed results.

5.1 Driving next to a wall

The first scenario we describe is driving next to a wall, which is acting as a reflector in the channel. As explained in the previous section, the wall reflector for our case will be the Ronald Tutor Hall building at USC. In general, driving next to a reflector is a scenario that can be observed in regular driving, where such a reflector can be a wall, an infrastructure, or even large reflective trailer truck. For this scenario, the Tx and the Rx were put in a bumper-to-bumper position for the reference measurement, after which the Rx was moved a distance of 8m from the Tx, and the channel was measured for an additional 7m. Therefore, at the end of the measurement scenario, the distance between the Tx and the Rx was 15m.

During the measurement, and as a stability check for the Tx rotation speed, we show first the Tx RPM vs time in the Fig. 18. We notice a very stable rotation speed at the Tx.

Fig. 19 shows both omni-directional power and directional power in the direction $(\phi_{0,Tx}(t), \phi_{0,Rx}(t))$ of the maximum power. We can see both of them have a stable-decreasing trend over time. This can be explained by the increase in distance between the 2 vehicles.

The directional RMS delay spread and its CDF distribution are shown in Fig. 20. We can see from Fig. 20a that the RMS delay spread is ranging between 1 and 2.5 ns, with median around 2.3ns.

Our next goal is to generate the APS for every MIMO snapshot, as explained in the section 3.3. A few

Figure 18: Wall: Tx RPM vs Time (Sliding Averaging Window)

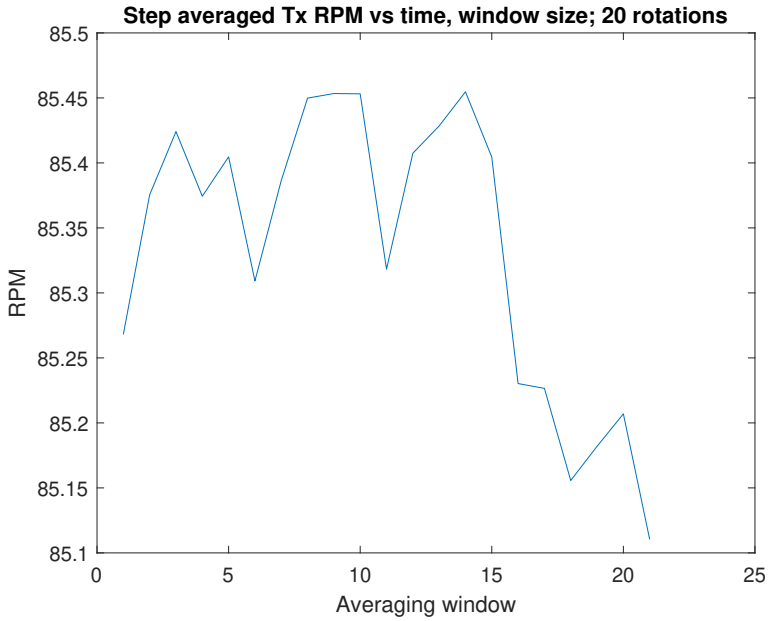

Figure 19: Wall: Omni and Directional Power Trend

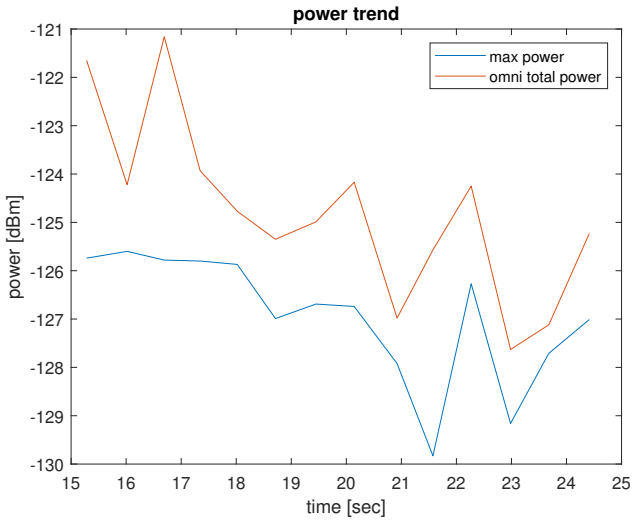

Figure 20: Wall: RMS Delay Spread and Corresponding CDF

(a) RMS Delay Spread

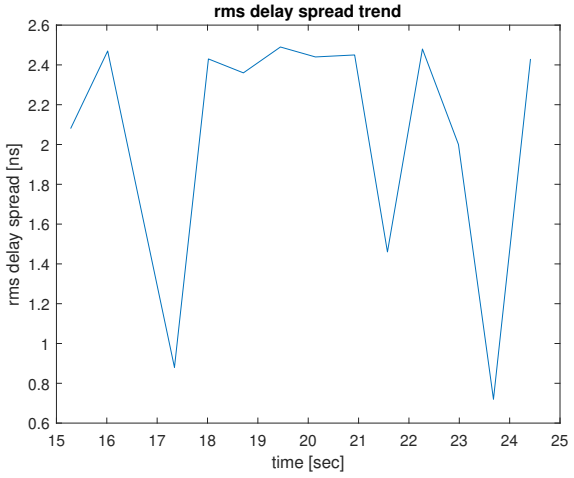

(b) RMS Delay Spread CDF

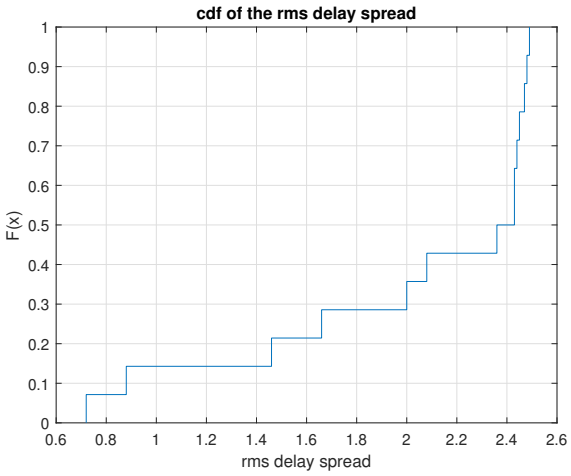

sample APSs are shown in Fig. 21, with a duration of 5 seconds between every sample APS. We can directly observe the existence of the wall reflection in almost every MIMO snapshot.

By the same method, after we process all the APS data for every MIMO snapshot, we get the angular spread on both link ends and their CDF distributions, which are shown in Fig. 22 and Fig. 23. Still, we can observe a very high angular spread at the Rx side. But we also notice that there is a decreasing trend in the angular spread at the end of the measurement for both sides. This can be explained as well by the increasing distance between the Tx and the Rx vehicles. The LoS path and the main reflected paths start to converge as departing and/or arriving from a similar direction.

5.2 In front and behind a truck

The second scenario is static, neither of the Tx or the Rx is moving through the entire measurement. Since there is a big truck between the transceivers, the LoS is heavily attenuated. However, there are other directions in which an MPC can still travel with significant power, that includes a possible reflection through the mini van on the other side of the road (please refer to the scenario description), or even signals traveling around the sides, of the truck. Because we do not have the Rx sensor information, it is impossible to determine the real DoD $= 0°$ and DoA $= 0°$, i.e. the direction where the multi-path with the most power is travelling from/to. However, we can still center our measurement around the dominant path and take it as our $(0°, 0°)$ direction, which is what we have done for the evaluations of this scenario.

During the measurement, and as a stability check for the Tx rotation speed, we show first the Tx RPM vs time, which looks as in the Fig. 24. We notice a very stable rotation speed at the Tx.

Figure 21: wall: Sample APS Every 5 Seconds of Measurement

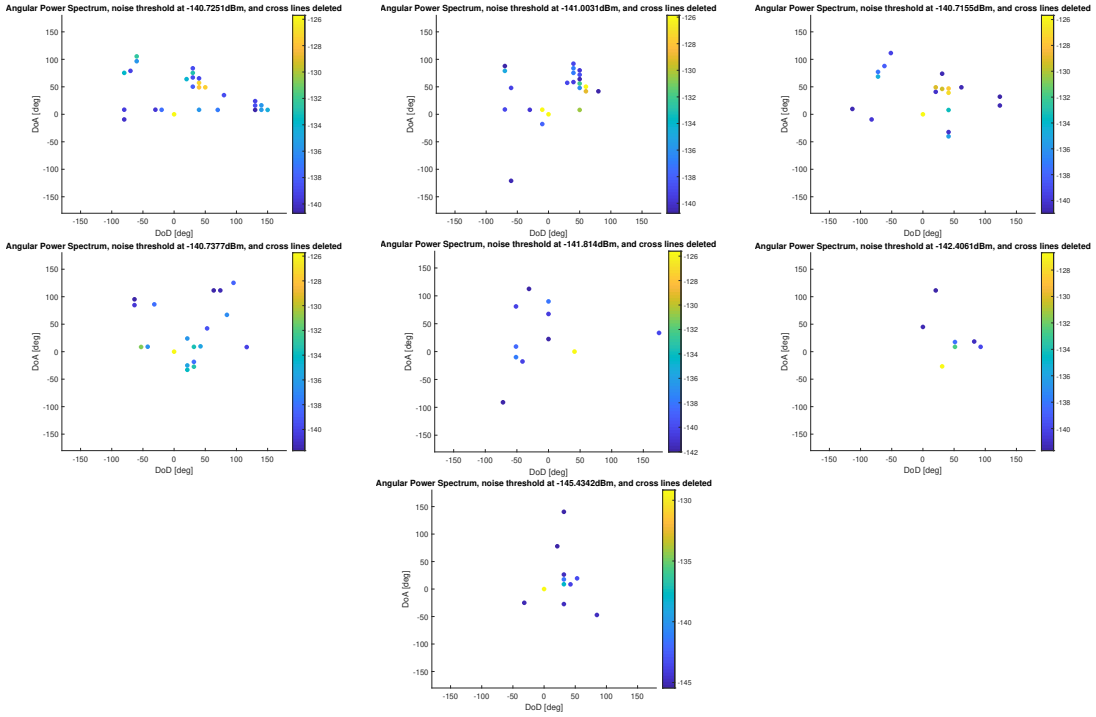

Figure 22: Wall: DOD Angular Spread and Corresponding CDF

(a) DOD Angular Spread

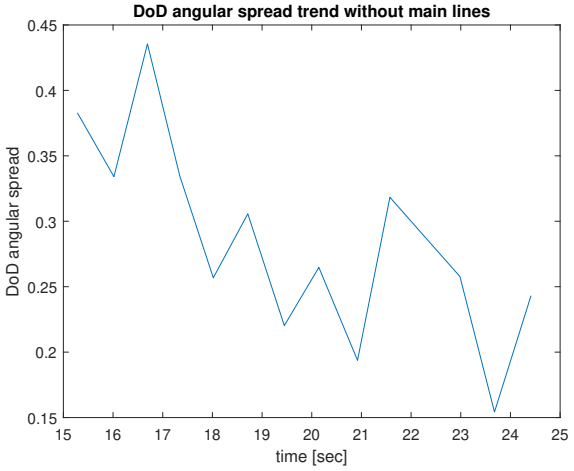

(b) DOD Angular Spread CDF

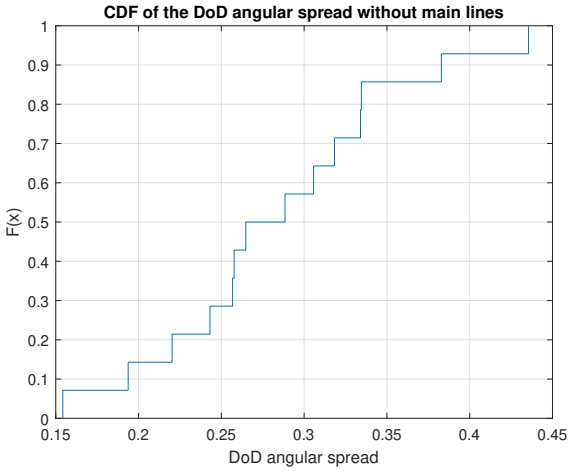

Figure 23: Wall: DOA Angular Spread and Corresponding CDF

(a) DOA Angular Spread

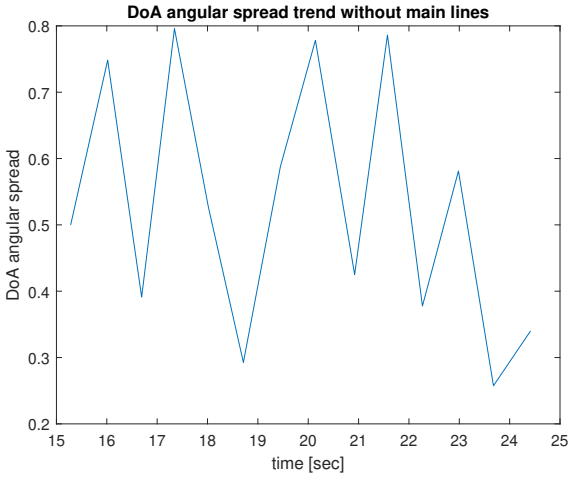

(b) DOA Angular Spread CDF

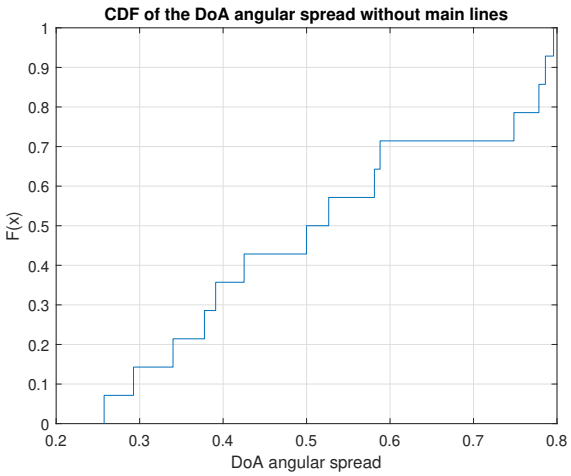

Figure 24: Truck: Tx RPM vs Time (Sliding Averaging Window)

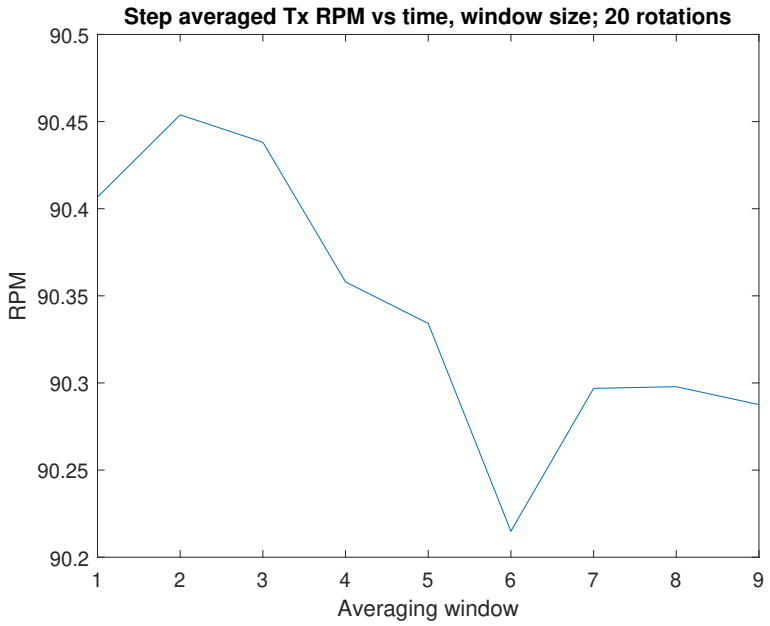

Figure 25: Truck: Omni and Directional Power Trend

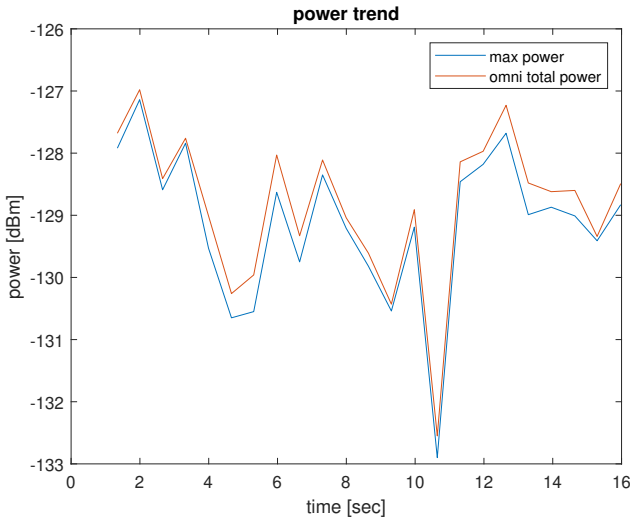

Figure 26: Truck: RMS Delay Spread and Corresponding CDF

(a) RMS Delay Spread

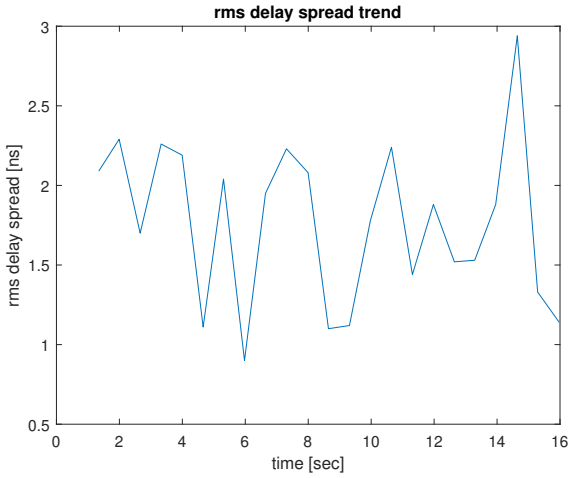

(b) RMS Delay Spread CDF

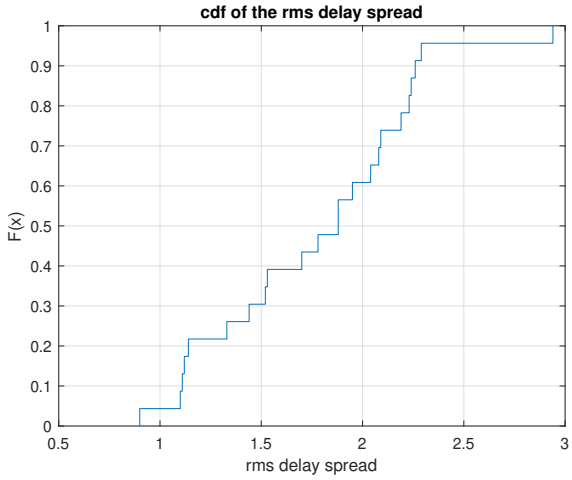

Fig. 25 shows the omni-directional power and maximum directional power vs time. The power, in particular the max-beam power, in this scenario shows some time variations despite the fact that neither TX nor RX was moving. In particular noticeable is the dip in the power at around 11 seconds into the measurement, which was due to a group of pedestrians walking into one of the reflected paths (the minivan path) during the measurement. We can also see the very similar pattern between the omni power and the max power plots, clearly stating that the maximum power path is the one responsible for majority of the total power received at the Rx.

Fig. 26 shows the directional RMS delay spread and the corresponding CDF distribution. Since there is no LoS path and a reflected path exists all the time, we do expect to see a higher RMS delay spread. We

Figure 27: Truck: Sample APS Every 5 Seconds of Measurement

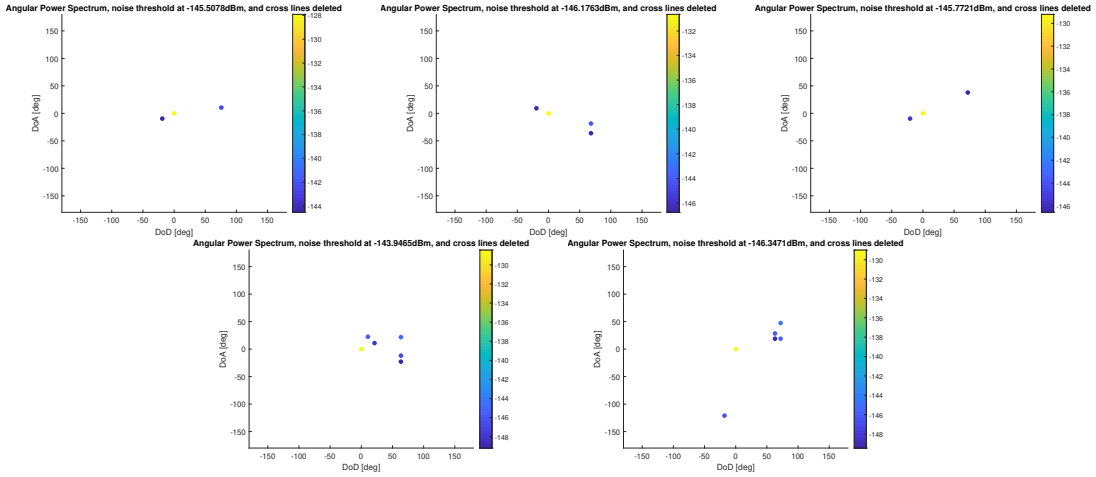

observe that the RMS delay spread is less than 3 ns for the duration of the measurement, with median of about 1.9 ns.

Figure 28: Truck: DOD Angular Spread and Corresponding CDF

(a) DOD Angular Spread

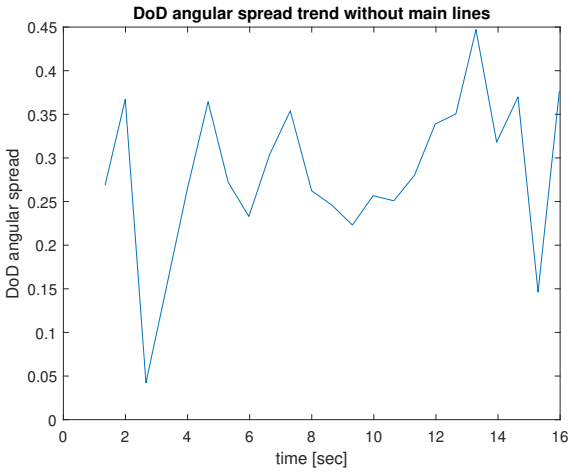

(b) DOD Angular Spread CDF

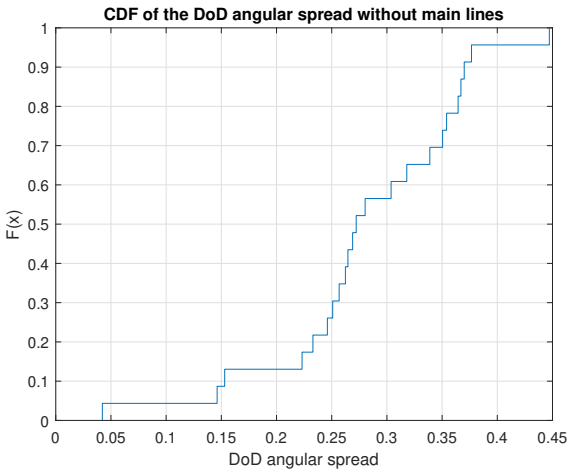

Fig. 27 shows the APS after the noise thresholding for this scenario. Fig. 28 and Fig. 29 show the angular spread on both link ends and their CDFs. Both DOA and DOD angular spreads seem to be low, and that is due to the low number of MPCs, as can be already seen from the sample APS plots. Remember that in this example the orientation of the (blocked) LOS cannot be identified, so that the absolute DoA and DoD are not aligned with the coordinate system. We rather conjecture that the components at 0/0 are dominant reflections.

Figure 29: Truck: DOA Angular Spread and Corresponding CDF

(a) DOA Angular Spread

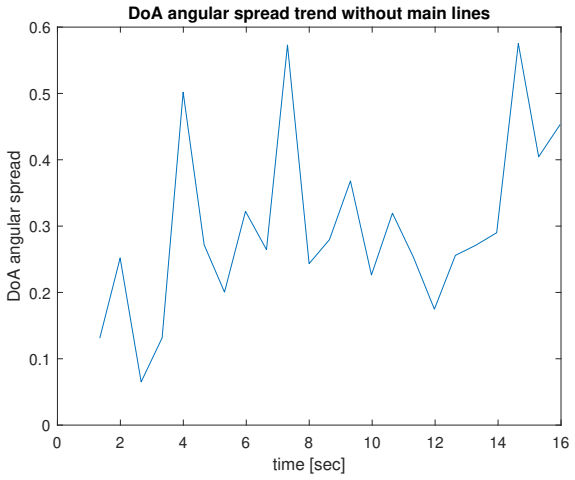

(b) DOA Angular Spread CDF

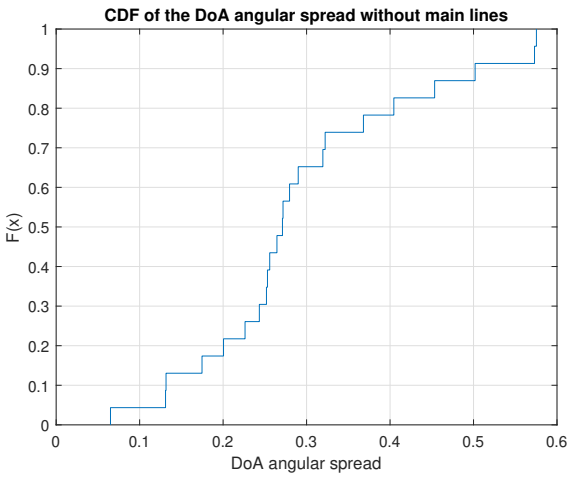

5.3 Mixed traffic scenario

In the mixed traffic scenario, we drive the cars in convoy, in an area with heavy load of traffic made from passenger cars, vans, and trucks. The Tx and the Rx started in a bumper-to-bumper position for the reference distance measurement, after which the Tx stays in position, and the Rx moves away from the Tx for a distance of 10 meters.

During the measurement, and as a stability check for the Tx rotation speed, we show first the Tx RPM vs time, which looks as in the Fig. 30. We notice a very stable rotation speed at the Tx.

Fig. 31 shows the omni-directional power and maximum directional power vs time. We notice that while the distance between the Tx and the Rx is increasing, both the omni and the max power curves have a decreasing trend, which can be explained by the propagation losses.

Figure 30: Traffic: Tx RPM vs Time (Sliding Averaging Window)

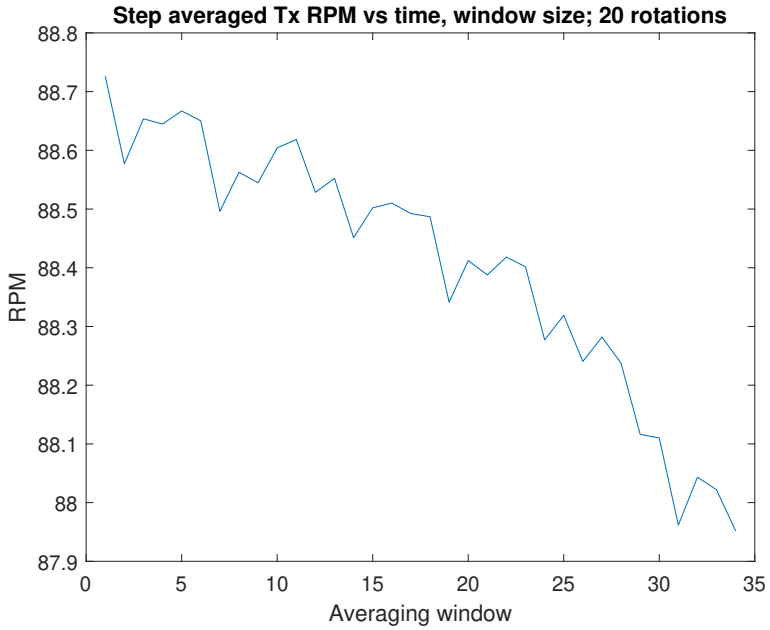

Figure 31: Traffic: Omni and Directional Power Trend

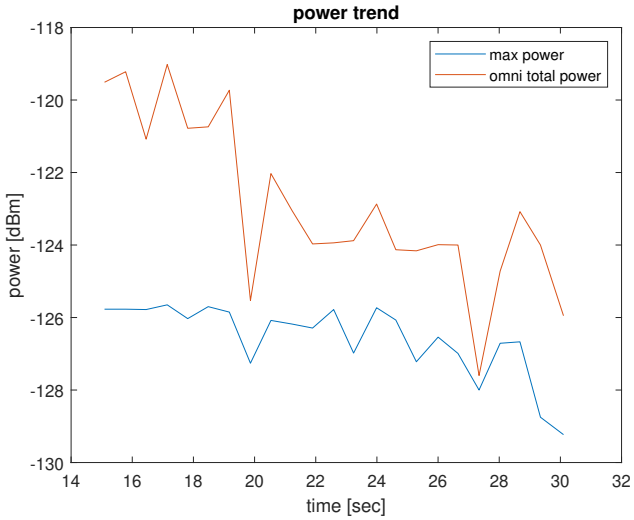

Figure 32: Traffic: RMS Delay Spread and Corresponding CDF

(a) RMS Delay Spread **(b) RMS Delay Spread CDF**

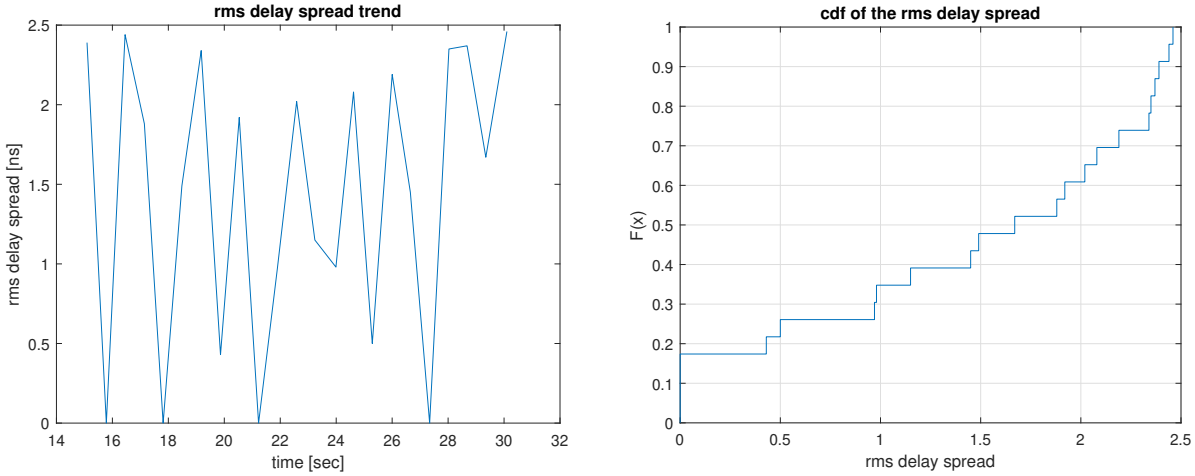

Figure 33: Traffic: Sample APS Every 5 Seconds of Measurement

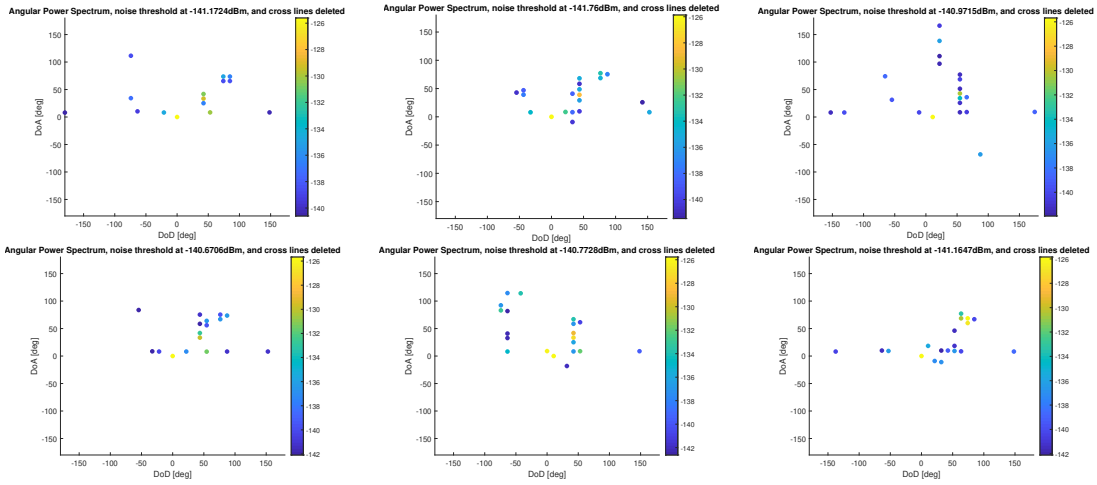

We observe the RMS delay spread and its corresponding CDF plot in Fig. 32. We observe a (directional) RMS delay spread of less than 2.5 ns. We can see from the CDF plot that the median of the RMS delay spread is about 1.6 ns.

A few sample APSs of the measurement every 5 seconds are shown in the Fig. 33. We can see from the APSs clearly the different MPCs with significant power, coming from the multiple reflections across the other vehicles surfaces.

Figure 34: Traffic: DOD Angular Spread and Corresponding CDF

(a) DOD Angular Spread

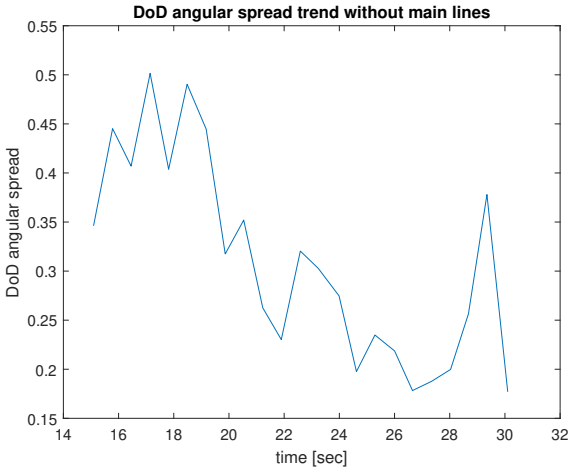

(b) DOD Angular Spread CDF

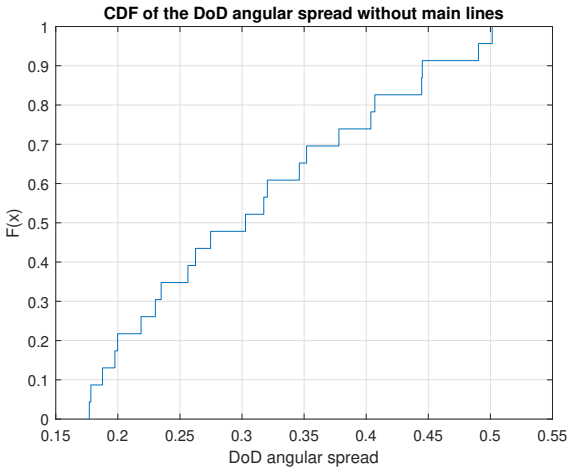

Figure 35: Traffic: DOA Angular Spread and Corresponding CDF

(a) DOA Angular Spread

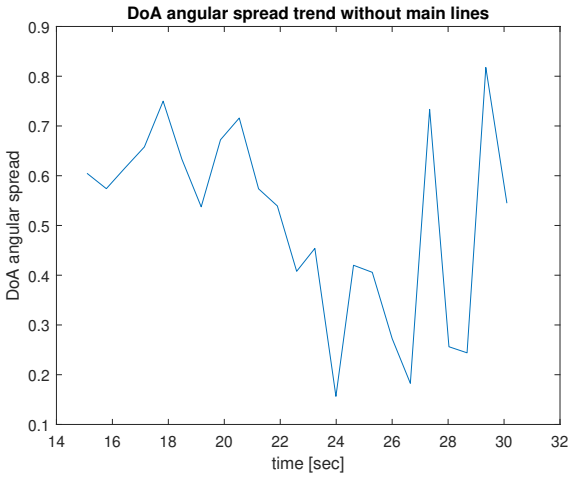

(b) DOA Angular Spread CDF

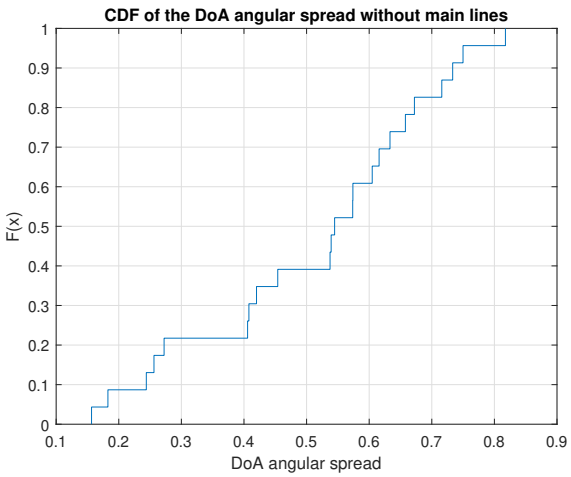

After generating the APSs corresponding to all MIMO snapshots, we calculate the angular spreads on both the Tx and the Rx and plot them in Fig. 34a and Fig. 35a. We observe a rather high angular spreads on both ends, which is due to the high density of reflectors situated all around the Tx and the Rx during this scenario.

6 Results from Collaboration

During the course of this project, we have done some work in collaboration with several institutions in Europe, in particular Technische Universitaet Wien, Austrian Institute of Technology, and Technical University Brno. The main emphasis of this part of the work was the measurement and modeling with fixed antennas (horns and/or omni-directional antennas), and the resulting channel statistics and models. This coordination of the measurement scenarios between different institutions was deemed desirable to cover a larger range of interesting situations. The majority of the work, including all the measurements themselves, was performed by the partner institutions; we contributed in the planning of the campaigns and the interpretation of the results. In the following we provide a brief summary of the main results; more details can be found in the cited papers.

Reference [30] deals with a V2V channel sounder for time-varying channels, operating in the 60 GHz band, but based on an omni-directional sounding approach. It permits a very large bandwidth measurement, 8 GHz in that paper; measurements were taken over a duration of a few seconds. Some work was also done on increasing the memory of that system to enable a longer duration as well. That sounder was used in [5] to model the scenario of vehicles passing each-others on a two-lane road, as can be seen in Fig. 36. We also show the normalized received power plot observed in that scenario, and the corresponding RMS delay spread. In Fig. 37b, every gray point represents one measured CIR and it can be easily noticed that the higher the received power, the higher the RMS delay spread. The blue crosses on the plot corresponds to the mean values of the RMS delay spread, while the variances in the corresponding datasets are depicted as the error bars.

Another sounder based on an omni-directional antenna at one link end and a horn antenna on the other was presented in [50], which has a 510 MHz bandwidth. It was then used in [49] to model the small and large scale fading during an overtaking scenario. This measurement describes the scenario when 2 vehicles are driving in convoy, communicating with a 60 GHz link. A third vehicle overtakes them and thus influences the wireless channel depending on its position, as shown in Fig. 38. The small-scale fading is modeled as a two-path with diffuse scattering model, and We show here 2 main parameters for this distribution, the K-factor (which is defined as the power ratio of the specular components to the diffuse components), and the parameter Δ which describes the amplitude relationship between the two specular components, being bounded between 0 and 1, where it's equal to 1 if and only if, the amplitudes of the specular components are equal. The modelling results are shown in Fig. 39.

In addition, the paper [16] reports a measurement in a V2I scenario, done in an urban street environment in downtown Vienna. The sounder used in that measurement was capable of sounding with a 100 MHz sounding waveform, and designed as a 2-horns antenna system at one link end, one horn radiating in the

Figure 36: Measurement Scenario - Passing Vehicles

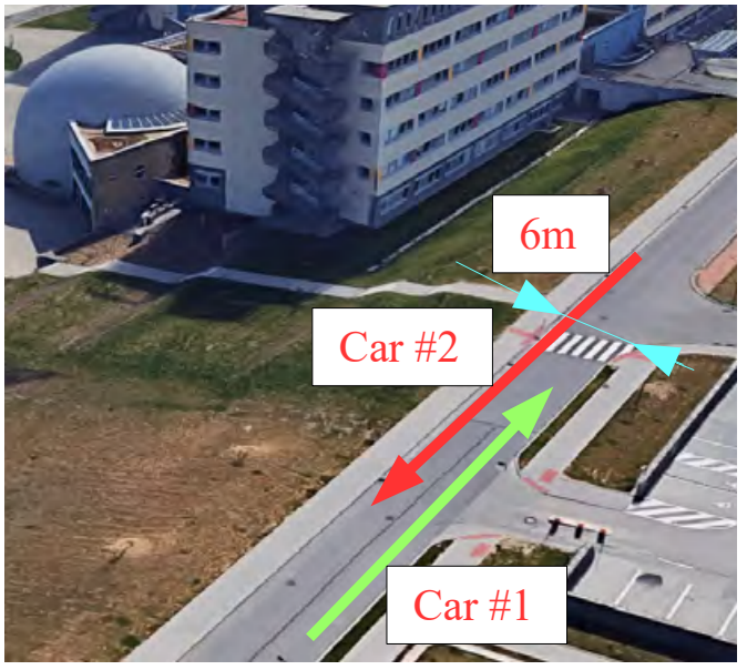

Figure 37: Power and RMS Delay Spread - Passing Vehicles

(a) Power Plot - Passing Vehicless

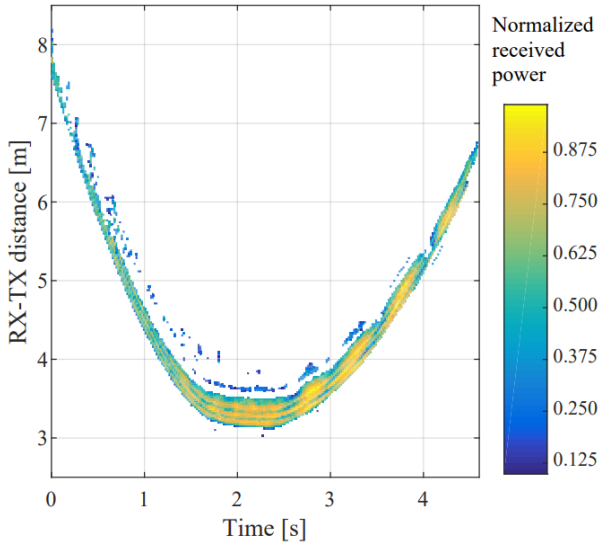

(b) RMS Delay Spread - Passing Vehicles

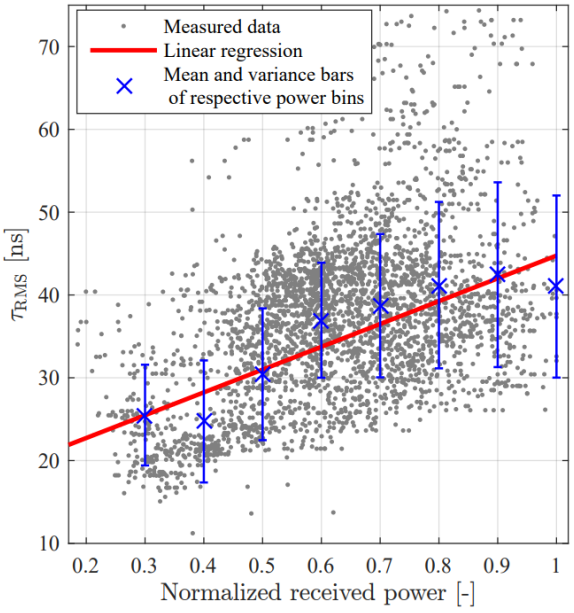

Figure 38: Measurement Scenario - Overtaking

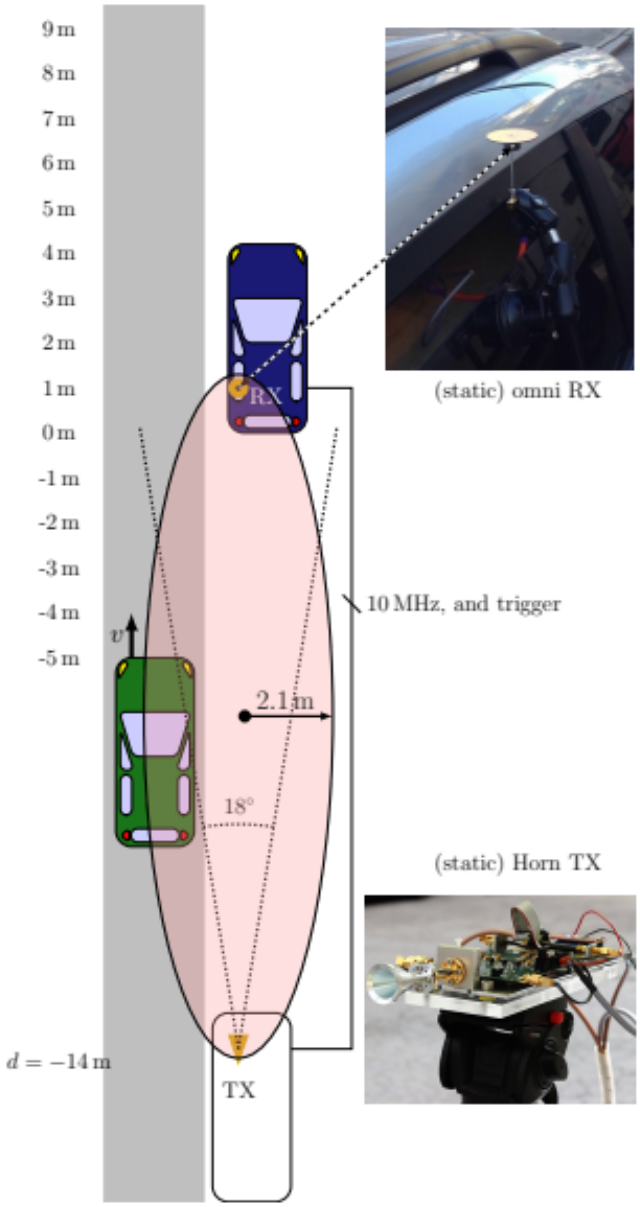

Figure 39: K and Delta factors - Overtaking

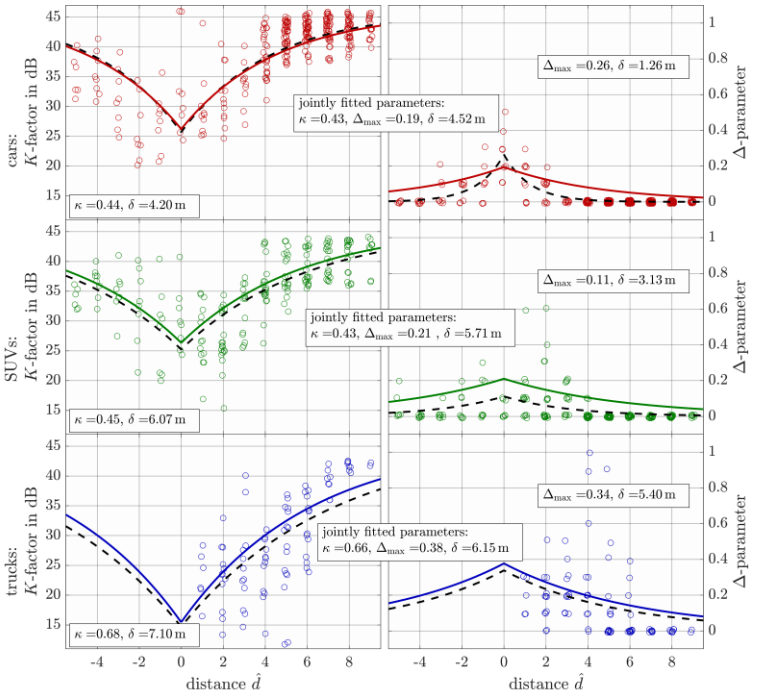

horizontal domain while the other horn is emitting the signal with an upward tilt of 15 degrees. Such a configuration helped in describing the impact of a beam elevation on the V2I communication channel characteristics, mainly the propagation losses and the scattering function in the delay-Doppler domain. We also used a similar sounder in [15] where the channel was measured at a crossroads in an urban environment, with the Tx being the 2-horn antenna system described earlier, mounted on a moving vehicle, and the Rx being an omni-directional antenna mounted on a crane arm, as shown in Fig. 40. We have shown in that publication how the channel transfer function amplitudes change in a typical vehicle trajectory in an urban street environment, with the use of 2 parameters, the SNR of the measurement, and the distribution of the magnitudes of the LOS delay taps, described as violin plots.

Another sounder is the one described in [29]. That sounder was based on an omni-directional antenna on the transmitter, mounted on top of a moving car, and a manually steered directional horn antenna on the receiver side, fixed on an infrastructure. A front view and an RX-Point-of-View figures are shown in Fig 41. In the Point-of-View of the Rx, we show the angular grid over which the evaluations were done, as seen in Fig 42. We noticed that the RMS delay spread for that scenario was always between 3 and 50 ns, and that there is no direct relationship between the RMS delay spread and the power plot, except in point 13 where we have the maximum for both these quantities.

Figure 40: Measurement Scenario - Crossroads

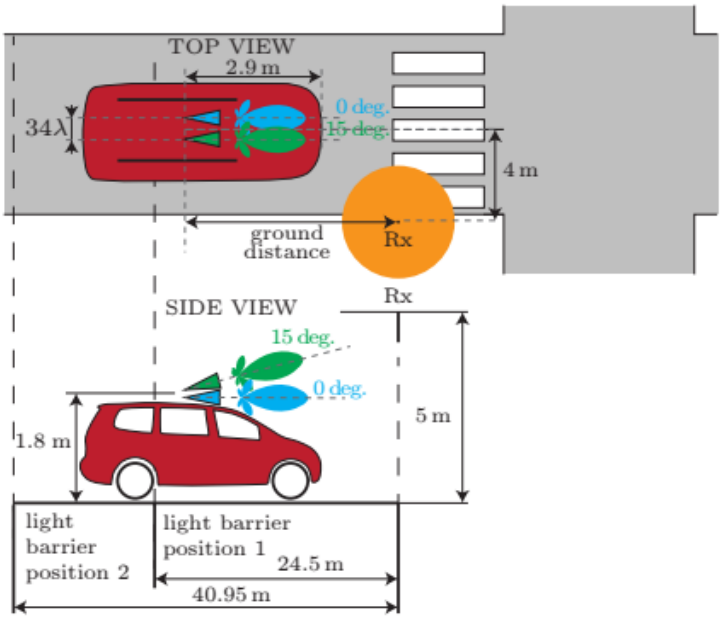

Figure 41: Measurement Scenario, TU Brno

(a) Front View Showing Both the Tx and the Rx (b) Rx Point-of-view

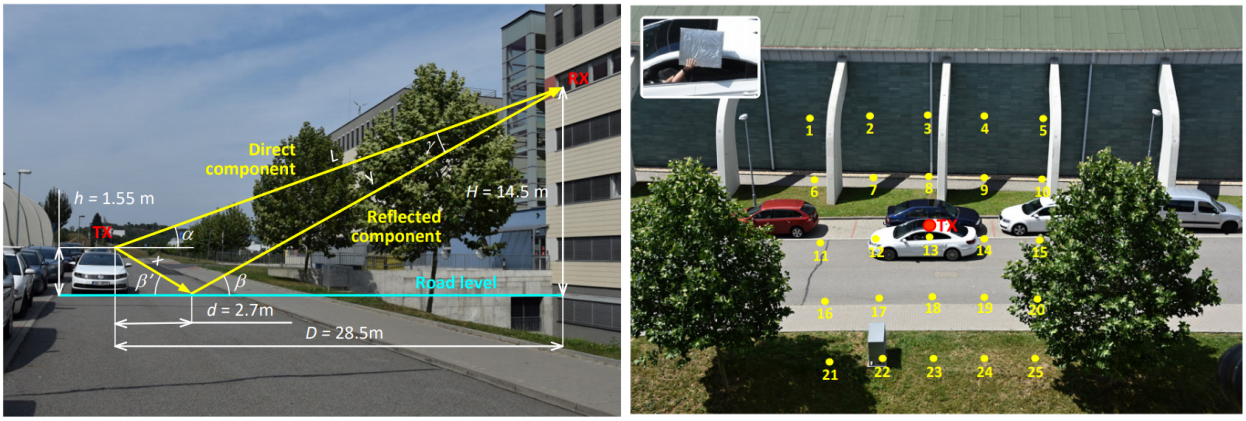

Figure 42: Measurement Scenario, TU Brno

(a) Power Grid Plot - TU Brno

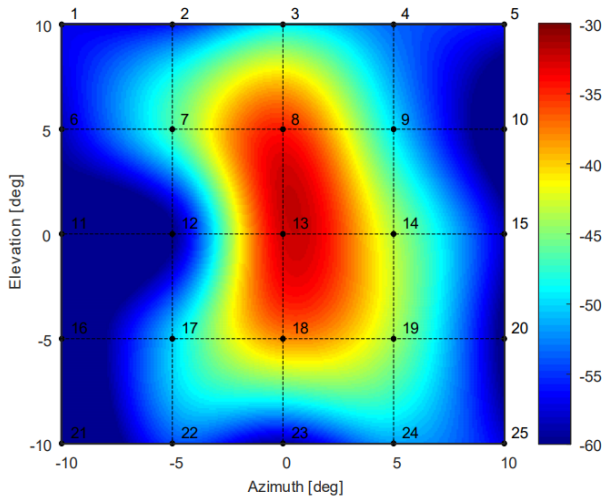

(b) RMS Delay Spread Plot - TU Brno

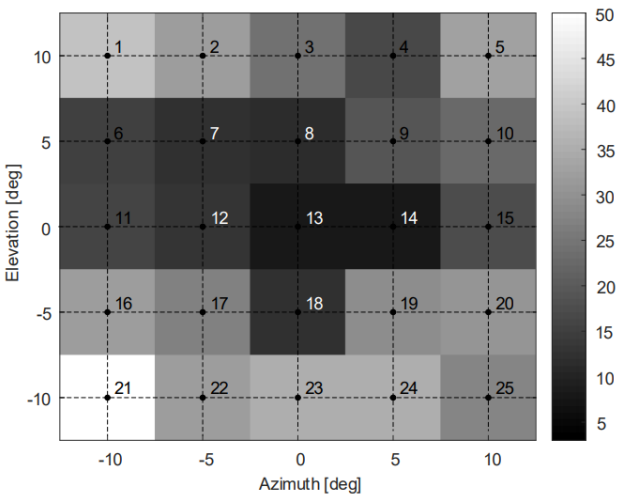

7 Conclusion

7.1 Summary of project's findings

In this project, we have investigated the characteristics of mmWave channels for V2V communications. After construction, calibration, and testing of a new channel sounder, we have performed measurements in a variety of environments, including both LOS and NLOS situations.

The results were marred by Covid-19 related difficulties, which prevented a timely re-doing of the campaigns after improvement of our setups. The presented results are impacted by various hardware problems, including a malfunctioning location sensor. While we extracted data through careful post-processing, and showed physically reasonable explanation for those results, all the extracted results must be taken with a grain (or a pitcher) of salt. Future re-measurements are discussed below.

The main extracted results refer to the directional rms delay spread, i.e., the delay spread that would be experienced if an adaptive antenna were to form the beam into the direction that provides the maximum power. This delay spread value is an important design parameter for V2V communication systems. We found that in most situations this directional delay spread is on the order of 1-3 ns. These values are very low, and it must be kept in mind that they are *directional* delay spreads, which are inherently lower than omni-directional delay spreads, and furthermore the distances between Tx and RX in our measurements were relatively short, which also tends to decrease delay spread values. We furthermore found that the angular spreads both at the TX and the RX can be quite significant. Even more importantly, we found that for the

case that the LOS between TX and RX is inhibited by another vehicle, e.g., a truck, reflections via other objects in the vicinity (house walls, other cars) can carry the most significant energy and allow to maintain communications. We stress that such insights cannot be easily obtained from the conventional "fixed-horn" measurements performed in previous mmWave V2V campaigns.

7.2 Future work

We have, in the lab, eliminated most of the hardware problems described (malfunctioning position sensor, reduction of the timing jitter by replacing software interrupts by hardware interrupts). Thus, the next planned stage of our work is to re-calibrate the new setup, and then re-do not only the scenarios described here, but perform measurements with longer trajectories and stronger variations of the distance between the TX and RX. While these measurements could not be performed before the due date of the final report, we will still execute them and publish the results in suitable journals and/or conferences, and will provide the details of the results to METRANS.

References

[1] Taimoor Abbas, Johan Karedal, Fredrik Tufvesson, Alexander Paier, Laura Bernadó, and Andreas F Molisch. Directional analysis of vehicle-to-vehicle propagation channels. In *Vehicular Technology Conference (VTC Spring), 2011 IEEE 73rd*, pages 1–5. IEEE, 2011.

[2] G. Acosta-Marum and M. A. Ingram. Six time- and frequency- selective empirical channel models for vehicular wireless LANs. 2(4):4–11, 2007.

[3] L. Bernado, T. Zemen, F. Tufvesson, A.F. Molisch, and C.F. Mecklenbrauker. The (in-) validity of the WSSUS assumption in vehicular radio channels. In *Personal Indoor and Mobile Radio Communications (PIMRC), 2012 IEEE 23rd International Symposium on*, pages 1757–1762, Sept 2012.

[4] L. Bernado, T. Zemen, F. Tufvesson, A.F. Molisch, and C.F. Mecklenbrauker. Delay and Doppler spreads of nonstationary vehicular channels for safety-relevant scenarios. *Vehicular Technology, IEEE Transactions on*, 63(1):82–93, Jan 2014.

[5] Jiri Blumenstein, Ales Prokes, Josef Vychodil, Tomas Mikulasek, Erich Zochmann, Herbert Groll, Christoph F Mecklenbrauker, Markus Hofer, Thomas Zemen, Seun Sangodoyin, et al. Vehicle-to-vehicle millimeter-wave channel measurements at 56-64 ghz. In *2019 IEEE 90th Vehicular Technology Conference (VTC2019-Fall)*, pages 1–5. IEEE, 2019.

[6] Mate Boban, Diego Dupleich, Naveed Iqbal, Jian Luo, Christian Schneider, Robert Müller, Ziming Yu, David Steer, Tommi Jämsä, Jian Li, et al. Multi-band vehicle-to-vehicle channel characterization in the presence of vehicle blockage. *IEEE Access*, 7:9724–9735, 2019.

[7] Mate Boban, Apostolos Kousaridas, Konstantinos Manolakis, Joseph Eichinger, and Wen Xu. Use cases, requirements, and design considerations for 5g v2x. *arXiv preprint arXiv:1712.01754*, 2017.

[8] Mate Boban, Konstantinos Manolakis, Mohamed Ibrahim, Samer Bazzi, and Wen Xu. Design aspects for 5g v2x physical layer. In *Standards for Communications and Networking (CSCN), 2016 IEEE Conference on*, pages 1–7. IEEE, 2016.

[9] L. Cheng, B.E. Henty, D.D. Stancil, F. Bai, and P. Mudalige. Mobile vehicle-to-vehicle narrow-band channel measurement and characterization of the 5.9 GHz dedicated short range communication (DSRC) frequency band. 25:1501–1516, 2007.

[10] J. Choi, V. Va, N. Gonzalez-Prelcic, R. Daniels, C. R. Bhat, and R. W. Heath. Millimeter-wave vehicular communication to support massive automotive sensing. *IEEE Communications Magazine*, 54(12):160–167, December 2016.

[11] Aditya Chopra, Andrew Thornburg, Ojas Kanhere, Abbas Termos, Saeed S Ghassemzadeh, and

Theodore S Rappaport. Real-time millimeter wave omnidirectional channel sounder using phased array antennas. In *IEEE Globecom 2020*, 2020.

[12] B. H. Fleury. First- and second-order characterization of direction dispersion and space selectivity in the radio channel. *IEEE Transactions on Information Theory*, 46(6):2027–2044, 2000.

[13] M. Giordani, T. Shimizu, A. Zanella, T. Higuchi, O. Altintas, and M. Zorzi. Path loss models for v2v mmwave communication: Performance evaluation and open challenges. In *2019 IEEE 2nd Connected and Automated Vehicles Symposium (CAVS)*, pages 1–5, 2019.

[14] Marco Giordani, Andrea Zanella, and Michele Zorzi. Millimeter wave communication in vehicular networks: Challenges and opportunities. In *Modern Circuits and Systems Technologies (MOCAST), 2017 6th International Conference on*, pages 1–6. IEEE, 2017.

[15] H Groll, E Zöchmann, M Hofer, H Hammoud, S Sangodoyin, T Zemen, J Blumenstein, A Prokes, AF Molisch, and CF Mecklenbräuker. 60 ghz v2i channel variability for different elevation angle switching strategies. In *2020 14th European Conference on Antennas and Propagation (EuCAP)*, pages 1–5. IEEE, 2020.

[16] Herbert Groll, Erich Zöchmann, Stefan Pratschner, Martin Lerch, Daniel Schützenhöfer, Markus Hofer, Jiri Blumenstein, Seun Sangodoyin, Thomas Zemen, Ales Prokes, et al. Sparsity in the delay-doppler domain for measured 60 ghz vehicle-to-infrastructure communication channels. *arXiv preprint arXiv:1901.10817*, 2019.

[17] Ruisi He, Bo Ai, Gongpu Wang, Zhangdui Zhong, Christian Schneider, Diego A Dupleich, Reiner S Thomae, Mate Boban, Jian Luo, and Yunyong Zhang. Propagation channels of 5g millimeter-wave vehicle-to-vehicle communications: recent advances and future challenges. *IEEE vehicular technology magazine*, 15(1):16–26, 2019.

[18] Marc Heddebaut, Fouzia Elbahhar, Christophe Loyez, Nizar Obeid, Nathalie Rolland, Atika Rivenq, and Jean-Michel Rouvaen. Millimeter-wave communicating-radars for enhanced vehicle-to-vehicle communications. *Transportation Research Part C: Emerging Technologies*, 18(3):440–456, 2010.

[19] E. Kampert, P. A. Jennings, and M. D. Higgins. Investigating the v2v millimeter-wave channel near a vehicular headlight in an engine bay. *IEEE Communications Letters*, 22(7):1506–1509, 2018.

[20] J. Kunisch and J. Pamp. Wideband car-to-car radio channel measurements and model at 5.9 GHz. 2008.

[21] L. Liang, H. Peng, G. Y. Li, and X. Shen. Vehicular communications: A physical layer perspective. *IEEE Transactions on Vehicular Technology*, 66(12):10647–10659, Dec 2017.

[22] Christoph F Mecklenbrauker, Andreas F Molisch, Johan Karedal, Fredrik Tufvesson, Alexander Paier,

Laura Bernado, Thomas Zemen, Oliver Klemp, and Nicolai Czink. Vehicular channel characterization and its implications for wireless system design and performance. *Proceedings of the IEEE*, 99(7):1189–1212, 2011.

[23] Andreas F Molisch, Fredrik Tufvesson, Johan Karedal, and C Mecklenbrauker. A survey on vehicle-to-vehicle propagation channels. *Wireless Communications, IEEE*, 16(6):12–22, 2009.

[24] A. Paier, J. Karedal, N. Czink, C. Dumard, T. Zemen, F. Tufvesson, A.F. Molisch, and C. F. Mecklenbräuker. Characterization of vehicle-to-vehicle radio channels from measurements at 5.2GHz. 50:19–29, 2009.

[25] J. Park, J. Lee, K. Kim, K. Lee, and M. Kim. Vehicle antenna position dependent path loss for millimeter-wave v2v communication. In *2018 11th Global Symposium on Millimeter Waves (GSMM)*, pages 1–3, 2018.

[26] Panagiotis Paschalidis, Andreas Kortke, Kim Mahler, Michael Peter, Mike Wisotzki, and Wilhelm Keusgen. Wideband car-to-car mimo radio channel measurements at 5.7 ghz in typical communication scenarios. In *Vehicular Technology Conference Fall (VTC 2009-Fall), 2009 IEEE 70th*, pages 1–5. IEEE, 2009.

[27] Cristina Perfecto, Javier Del Ser, Mehdi Bennis, and Miren Nekane Bilbao. Beyond wysiwyg: Sharing contextual sensing data through mmwave v2v communications. In *Networks and Communications (EuCNC), 2017 European Conference on*, pages 1–6. IEEE, 2017.

[28] V. Petrov, J. Kokkoniemi, D. Moltchanov, J. Lehtomäki, M. Juntti, and Y. Koucheryavy. The impact of interference from the side lanes on mmwave/thz band v2v communication systems with directional antennas. *IEEE Transactions on Vehicular Technology*, 67(6):5028–5041, 2018.

[29] Ales Prokes, Jiri Blumenstein, Josef Vychodil, Tomas Mikulasek, Roman Marsalek, Erich Zöchmann, Herbert Groll, Christoph F Mecklenbräuker, Thomas Zemen, Aniruddha Chandra, et al. Multipath propagation analysis for vehicle-to-infrastructure communication at 60 ghz. In *2019 IEEE Vehicular Networking Conference (VNC)*, pages 1–8. IEEE, 2019.

[30] Ales Prokes, Josef Vychodil, Tomas Mikulasek, Jiri Blumenstein, Erich Zöchmann, Herbert Groll, Christoph F Mecklenbräuker, Markus Hofer, David Löschenbrand, Laura Bernadó, et al. Time-domain broadband 60 ghz channel sounder for vehicle-to-vehicle channel measurement. In *2018 IEEE Vehicular Networking Conference (VNC)*, pages 1–7. IEEE, 2018.

[31] Theodore S Rappaport, Robert W Heath Jr, Robert C Daniels, and James N Murdock. *Millimeter wave wireless communications*. Pearson Education, 2014.

[32] O. Renaudin, V. M. Kolmonen, P. Vainikainen, and C. Oestges. Wideband MIMO car-to-car radio channel measurements at 5.3 GHz. 2008.

[33] Olivier Renaudin. *Experimental channel characterization for vehicle-to-vehicle communication systems*. PhD thesis, Universite Catholique de Lovain, Belgium, 2013.

[34] Olivier Renaudin, Veli-Matti Kolmonen, Pertti Vainikainen, and Claude Oestges. Wideband measurement-based modeling of inter-vehicle channels in the 5-ghz band. *IEEE Transactions on Vehicular Technology*, 62(8):3531–3540, 2013.

[35] Y. Sadovaya, D. Solomitckii, W. Mao, O. Orhan, H. Nikopour, S. Talwar, S. Andreev, and Y. Koucheryavy. Geometry-based v2v channel modeling over millimeter-wave in highway scenarios. In *2019 11th International Congress on Ultra Modern Telecommunications and Control Systems and Workshops (ICUMT)*, pages 1–6, 2019.

[36] Y. Sadovaya, D. Solomitckii, W. Mao, O. Orhan, H. Nikopour, S. Talwar, S. Andreev, and Y. Koucheryavy. Ray-based modeling of directional millimeter-wave v2v transmissions in highway scenarios. *IEEE Access*, 8:54482–54493, 2020.

[37] Kei Sakaguchi, Thomas Haustein, Sergio Barbarossa, Emilio Calvanese Strinati, Antonio Clemente, Giuseppe Destino, Aarno Pärssinen, Ilgyu Kim, Heesang Chung, Junhyeong Kim, et al. Where, when, and how mmwave is used in 5g and beyond. *IEICE Transactions on Electronics*, 100(10):790–808, 2017.

[38] K. Sato and M. Fujise. Propagation measurements for inter-vehicle communication in 76-ghz band. In *2006 6th International Conference on ITS Telecommunications*, pages 408–411, June 2006.

[39] W. Schaefer. Channel modelling of short-range radio links at 60 ghz for mobile intervehicle communication. In *Vehicular Technology Conference, 1991. Gateway to the Future Technology in Motion., 41st IEEE*, pages 314–319, May 1991.

[40] W. Schafer. A new deterministic/stochastic approach to model the intervehicle channel at 60 ghz. In *Vehicular Technology Conference, 1993., 43rd IEEE*, pages 112–115, May 1993.

[41] R. Schneider, D. Didascalou, and W. Wiesbeck. Impact of road surfaces on millimeter-wave propagation. *IEEE Transactions on Vehicular Technology*, 49(4):1314–1320, Jul 2000.

[42] I. Sen and D.W. Matolak. Vehicle–vehicle channel models for the 5-GHz band. 9(2):235–245, 2008.

[43] S. Takahashi, A. Kato, K. Sato, and M. Fujise. Distance dependence of path loss for millimeter wave inter-vehicle communications. In *Vehicular Technology Conference, 2003. VTC 2003-Fall. 2003 IEEE 58th*, volume 1, pages 26–30 Vol.1, Oct 2003.

[44] Vutha Va, Takayuki Shimizu, Gaurav Bansal, Robert W Heath Jr, et al. Millimeter wave vehicular communications: A survey. *Foundations and Trends® in Networking*, 10(1):1–113, 2016.

[45] Hui Wang, Xuefeng Yin, Xuesong Cai, Haowen Wang, Ziming Yu, and Juyul Lee. Fading characteriza-

tion of 73 ghz millimeter-wave v2v channel based on real measurements. In *International Workshop on Communication Technologies for Vehicles*, pages 159–168. Springer, 2018.

[46] R. Wang, O. Renaudin, C. U. Bas, S. Sangodoyin, and A. F. Molisch. High-resolution parameter estimation for time-varying double directional v2v channel. *IEEE Transactions on Wireless Communications*, 16(11):7264–7275, Nov 2017.

[47] A. Yamamoto, K. Ogawa, T. Horimatsu, A. Kato, and M. Fujise. Path-loss prediction models for intervehicle communication at 60 ghz. *IEEE Transactions on Vehicular Technology*, 57(1):65–78, Jan 2008.

[48] A. Yamamoto, K. Ogawa, T. Horimatsu, K. Sato, and M. Fujise. Effect of road undulation on the propagation characteristics of inter-vehicle communications in the 60 ghz band. In *IEEE/ACES International Conference on Wireless Communications and Applied Computational Electromagnetics, 2005.*, pages 841–844, April 2005.

[49] Erich Zöchmann, Herbert Groll, and Stefan Pratschner. A small-scale fading model for overtaking vehicles in a millimeter wave communication link. In *2019 IEEE 20th International Workshop on Signal Processing Advances in Wireless Communications (SPAWC)*, pages 1–5. IEEE, 2019.

[50] Erich Zöchmann, Markus Hofer, Martin Lerch, Stefan Pratschner, Laura Bernadó, Jiri Blumenstein, Sebastian Caban, Seun Sangodoyin, Herbert Groll, Thomas Zemen, et al. Position-specific statistics of 60 ghz vehicular channels during overtaking. *Ieee Access*, 7:14216–14232, 2019.

Data Management Plan

Due to the limitations in our measurement data and the hardware errors that were described throughout the report, the collected data cannot be shared at this point in time. As the plan is to repeat the measurement campaign with the improved setup as soon as the COVID-19 situation is resolved, we will be sharing the new measurement data once that is available.